COURSE 1

GAMMA-RAY BURSTS

FRÉDÉRIC DAIGNE

Institut d'Astrophysique de Paris
98 bis boulevard Arago
75014 Paris France

PHOTO: height 7.5cm, width 11cm

Contents

GAMMA-RAY BURSTS

Frédéric Daigne[1]

Abstract

This lecture is an introduction to the study of gamma-ray bursts. Observations of the burst and its afterglow are first reviewed, with the identification of a few key observationnal facts that lead to a three-step theoretical scenario. The physical processes at work in each step are then presented, focussing on the internal / external shock model. The last part briefly mention the possible non-photonic emission of gamma-ray bursts.

1 Introduction

Gamma-ray bursts (hereafter GRBs) have been discovered by the *VELA* satellites at the end of the 60's [1]. A GRB is a short (from a few milliseconds to a few hundreds seconds) but very intense (peak flux up to hundreds of photons per square centimeters and per second) burst of gamma-rays (typically between 100 keV and 1 MeV). After their discovery, GRBs have been observed by many satellites with gamma-ray capabilities. I will not review here the results obtained in the 70's and the 80's. At the end of this period, the total number of detected GRBs was about five hundreds but the GRB distance scale remained undetermined, due to the poor localization capabilities of gamma-ray instruments which did not allow the identification of any counterpart. In most models, GRBs were related to Galactic neutron stars and the apparent isotropy of the GRB distribution was interpreted as a lack of sensibility, limiting the detection to local sources only. It was then believed that the next generation of detectors, thanks to a better sensibility, would show an accumulation of GRBs in the Galactic disk.
The *Burst And Transient Source Experiment* was launched on board the *Compton Gamma-Ray Observatory* in 1991 and observed GRBs until 2000 with a much better sensibility than all previous detectors. *BATSE* detected about one GRB per day during nine years and provided us with a catalog of about three thousands bursts. The most important *BATSE* result is prob-

[1]Institut d'Astrophysique de Paris, France

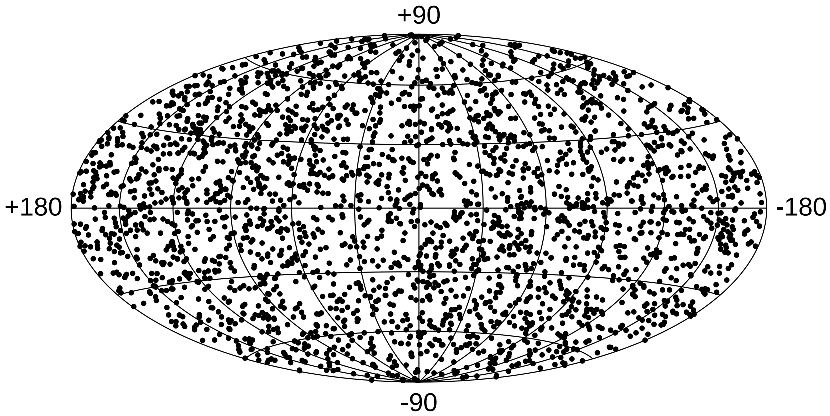

Fig. 1. Skymap of the 2704 BATSE GRBs in galactic coordinates (from [2]).

ably that despite the detection of much weaker GRBs, the distribution over the sky remained almost perfectly isotropic (see figure 1). This was the first strong evidence in favor of an extragalactic origin of GRBs.
The next major step was achieved in 1997 thanks to the *Beppo-SAX* satellite which discovered the X-ray afterglow of GRBs, i.e. a X-ray fading counterpart detected a few hours after the burst. This X-ray afterglow could be localized by *Beppo-SAX* with an accuracy of about one arcminute (instead of a few degrees in gamma-rays) and the corresponding position was distributed in ground-based observatories within a delay of a few hours. This led to the discovery of fading counterparts at other wavelengths : the optical and radio afterglows. The identification of highly redshifted absorption and emission lines in the spectrum of the optical afterglow and/or its host galaxy is the direct proof that GRBs are produced at cosmological distances (observed redshifts $z \sim 0.3$–4.5).
This direct determination of the distance scale has allowed rapid progress in the physical understanding of GRBs. Today most of the about 130 models of GRBs which were listed in 1994 [3] have been eliminated and only a few models remain, which sometimes differ only by one aspect of the theoretical scenario (for instance the central source).
In this lecture, I will first review the main observed properties of GRBs (section 2), starting from 1991 and the results of *BATSE*. Then I will describe the three step theoretical scenario which is adopted by most models (section 3). The three next sections will introduce the basic concepts for each of this three steps in the context of the most-discussed model, often called the fireball model. Section 7 will briefly discuss the very interesting possibility that GRBs may be the source of non-photonic emission (cosmic rays, neutrinos and gravitational waves). The conclusions in the last section

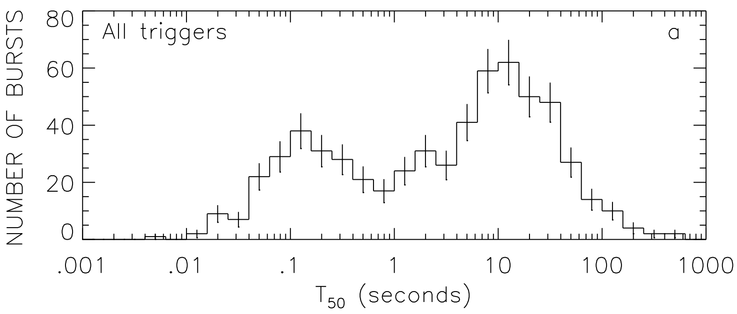

Fig. 2. Number of GRBs as a function of their duration (from [2]).

will mainly list the most important theoretical issues that are unsolved and describe the promising observational prospects in the field.

2 Observations

2.1 Prompt emission

Apart from the gamma-rays, the prompt emission (i.e. the burst itself) has been observed in X-rays in a few cases and in no other spectral band, with the notable exception of GRB 990123[1] were an optical flash was also detected. In this subsection I summarize the main properties of this prompt emission, focussing for the gamma-rays on the results of *BATSE*, which, from 1991 to 2000, has observed 2704 GRBs (not including un-triggered events), corresponding to a rate of about one event per day.

2.1.1 Duration

Figure 2 shows the distribution of the GRB duration T_{90} in the *BATSE* catalog. The duration T_{90} is defined as $T_{90} = t_{95} - t_5$, where t_{95} (resp. t_5) is the time at which 95 % (resp. 5 %) of the total fluence in the 2+3 *BATSE* band (50-300 keV) has been received. This duration is about 1-5 ms for the shortest bursts and can reach 1000 s. It is clear in figure 2 that there are at least two groups of GRBs : a group of short GRBs (about one third of the total, typical duration $T_{90} \sim 100$ ms) and a group of long GRBs (about two thirds, typical duration $T_{90} \sim 10$ s). Figure 3 shows the burst hardness ratio as a function of the duration T_{90}. The hardness ratio is the ratio of the count number in a high energy band (here 320-7000 keV) over the count

[1] GRBs are usually named after the day they were detected, here the 23th January 1999, followed by a,b,c,d,... in case of several detections in the same day.

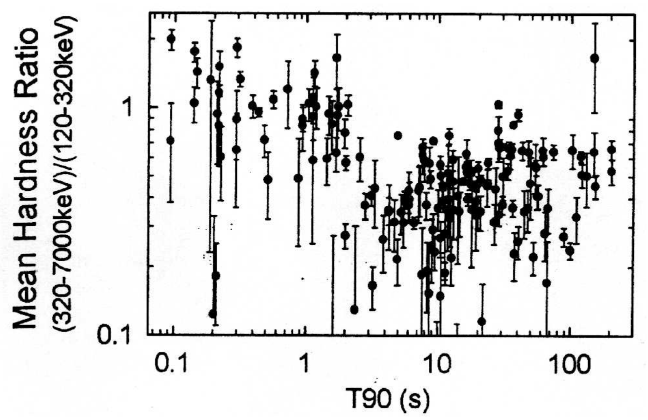

Fig. 3. Evolution of the hardness ratio with the burst duration (from [4]).

number in a low energy band (here 120-320 keV). This figure corresponds to GRBs observed with the PHEBUS experiment [4] but *BATSE* shows very similar results [5] : there is a clear evolution of the hardness from the group of short bursts to the group of long bursts, the short bursts being harder.

2.1.2 Time profile

One remarkable property of GRBs is the extreme diversity of their time profiles. A few examples are given in figure 4. Some time profiles are well structured, with a few well separated pulses (e.g. BATSE trigger 7469), whereas some others have extremely complex light curves (e.g. BATSE trigger 2533). However, it has been suggested that most of these profiles could be analysed as the sum of a few individual pulses [6]. An example of such a decomposition is given in figure 5. These individual pulses usually show an asymmetric profile with a fast rise and a slower decay. The pulse shape also changes with the duration, becoming more symmetric for small durations, and with the energy band : at high energy, the pulse peaks earlier and is narrower. This "pulse paradigm" can be quantified [6] : for instance the width $W(E)$ of the pulse at energy E is found to follow a power-law: $W(E) \propto E^{-0.4}$. In the X-ray range, the light curve is similar to what is observed in the gamma-ray range, the width of the pulses being even larger, as shown for example in figure 6. The possible X-ray precursors will be discussed later. A last important aspect to note is that the variability in the lightcurve appears to be present on several timescales and that the shortest timescales can be as short as 1 ms. This provides an important constraint for the models.

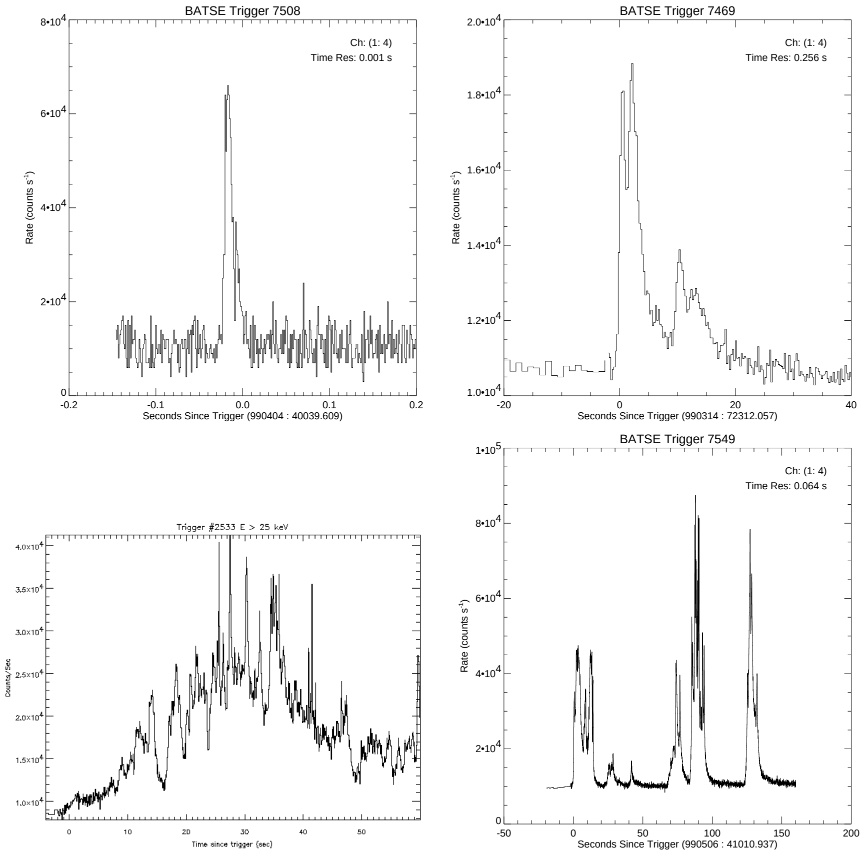

Fig. 4. A few GRB time profiles (from the BATSE catalog, [2])

2.1.3 Spectrum

The time-integrated GRB spectra do not show the same diversity as time profiles. They are non-thermal and are usally well fitted by the so-called GRB function [10] :

$$n\left(E\right)=\frac{E_{\gamma}}{E_{\mathrm{p}}^{2}}\times\mathcal{B}\left(\frac{E}{E_{\mathrm{p}}}\right)\ , \tag{2.1}$$

where E_{γ} is the total energy radiated in gamma-rays, E_{p} is the peak energy of the burst, i.e. the energy at which $E^2n(E)$ (or νF_{ν}) is maximum, and the function $\mathcal{B}(x)$ is made of two power-laws with a smooth transition :

$$\mathcal{B}(x)=\left\{\begin{array}{cc} x^{\alpha}\exp\left(-(2+\alpha)x\right) & x\le x_b \\ x^{\beta}x_b^{\alpha-\beta}\exp\left(-(2+\alpha)x_b\right) & x\ge x_{\mathrm{b}} \end{array}\right. \ . \tag{2.2}$$

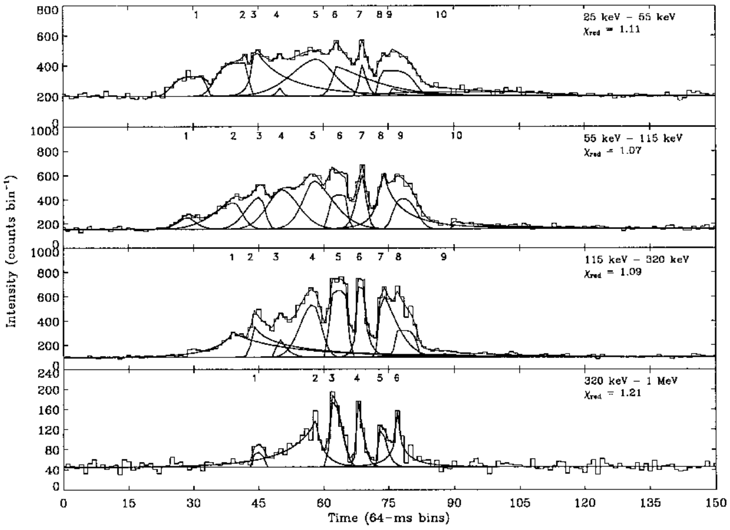

Fig. 5. Analysis of a complex GRB lightcurves as the sum of several pulses (BATSE data, from [6]).

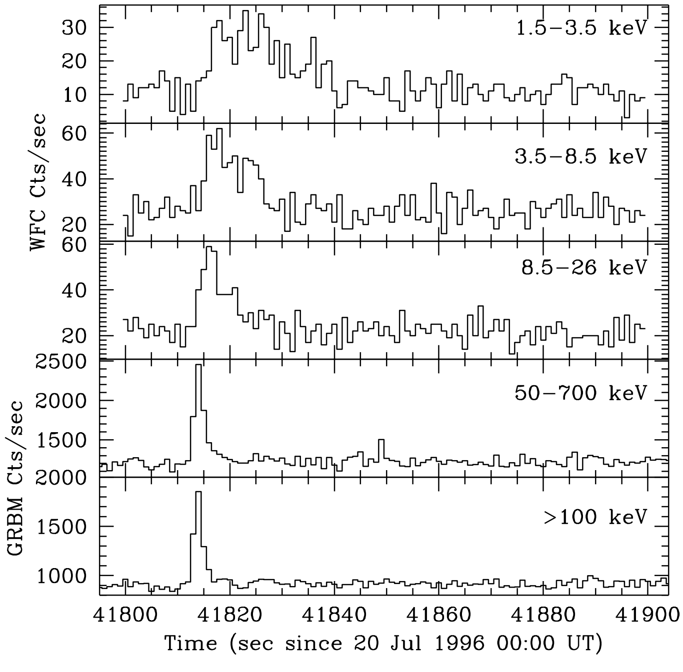

Fig. 6. Gamma- and X-ray profiles of GRB 960720 (Beppo-SAX data, from [7]).

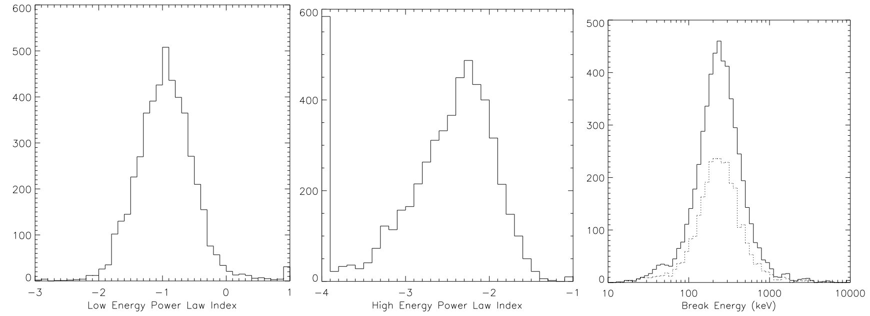

Fig. 7. Distribution of the low- and high-energy slopes and the break energy of the Band function (from [8]).

The transition occurs at $x_b = (\alpha - \beta)/(2 + \alpha)$. The distribution of the three parameters α, β and E_{p} (or the break energy $E_{\mathrm{b}} = x_b E_{\mathrm{p}}$) has been studied for a sample of long bright GRBs [8]. The results are plotted in figure 7. It is found that the averaged value of the low-energy and high-energy slopes

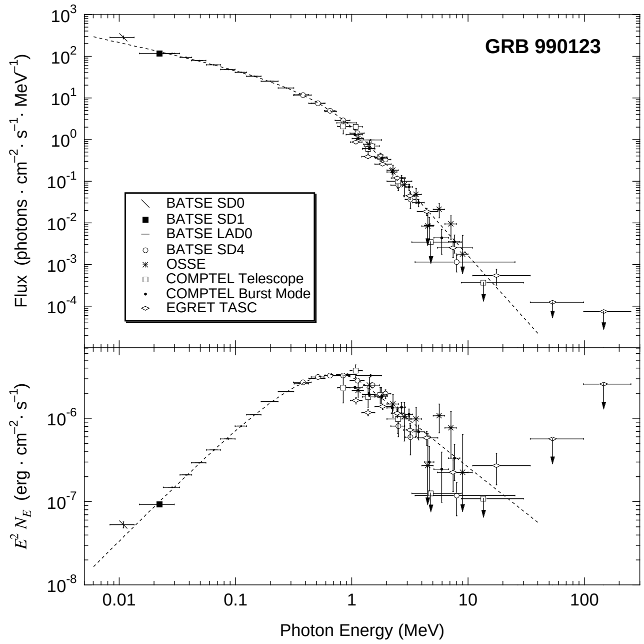

Fig. 8. The time integrated spectrum of GRB 990123 observed with the four instruments of CGRO : $\alpha \sim -0.6$, $\beta \sim -3.1$ and $E_{\mathrm{p}} \sim 720$ keV (from [9]).

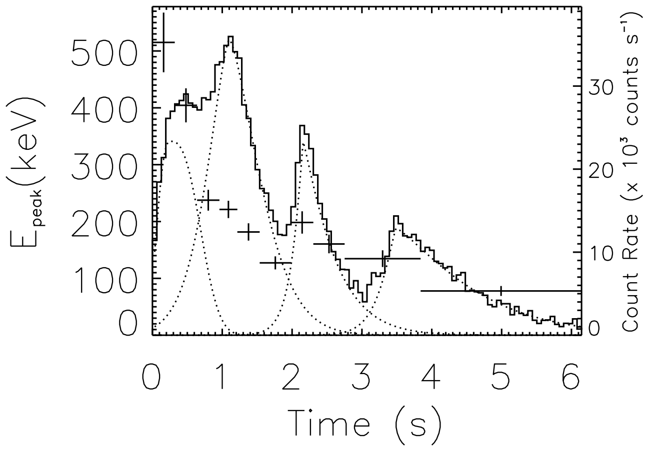

Fig. 9. The spectral evolution of BATSE trigger 543. A global hard-to-soft evolution as well as a hardness-intensity correlation in the decay phase of pulses are clearly identified. (from [11]).

are $\alpha \sim -1.0$ and $\beta = -2.25$ and that the break energy has a very narrow distribution, between 100 keV and 1 MeV. The spectrum of GRB 990123 is shown as an example in figure 8. Notice that this bright, long, hard burst has been detected by the four instruments of *CGRO*, up to about 10-20 MeV. The GRB function seems to fit correctly the spectrum over this whole spectral range, with no indication of high energy breaks that could be associated with the photon-photon annihilation. The lack of such a break will give another interesting constraint for the models. Notice also that no convicing line has ever been detected in the prompt emission spectrum.

2.1.4 Spectral evolution

The spectrum is strongly evolving during the burst. A global hard-to-soft evolution is observed in many GRBs (e.g. BATSE trigger 543 in figure 9), as well as a hardness-intensity (HIC) [12] and a hardness-fluence (HFC) [13] correlation in the decay phase of pulses :

$$E_{\rm p}(t) \propto N(t)^{\delta} \tag{2.3}$$

$$E_{\rm p}(t) \propto \exp\left(-\Phi(t)/\Phi_0\right)\ , \tag{2.4}$$

where $N(t)$ is the intensity (photon count number), $E_{\rm p}(t)$ is the peak energy at time t and

$$\Phi(t) = \int_0^t N(t')dt'$$

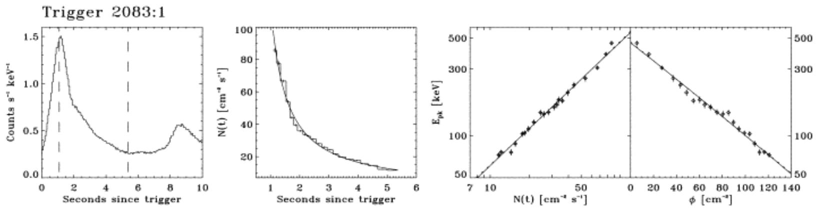

Fig. 10. The HFC and the HIC in the two pulses of BATSE trigger 2082 [15].

is the photon fluence. The index δ is usually smaller than unity. When these two correlations are verified, it can be shown that the intensity and the peak energy follow [14] :

$$N(t) = \frac{N(0)}{1+t/\tau} , \tag{2.5}$$

$$E_{\rm p}(t) = \frac{E_{\rm p}(0)}{\left(1+t/\tau\right)^{\delta}} , \tag{2.6}$$

where $\tau = \delta\Phi_0/N(0)$. This behaviour has been indeed observed in a sample of 25 long and bright GRBs verifying both the HIC and the HFC (see figure 10) [15]. Such a behaviour is a severe constraint for all models of the GRB prompt emission.

2.1.5 Optical flash

There is only one detection of the prompt emission of a GRB outside the X- and γ-ray bands. GRB 990123 was a long ($\sim$ 150 s) and very bright GRB and was observed by a robotic telescope (ROTSE) which succeeded in measuring the optical magnitude of the burst at three times before the end of the gamma-ray emission. The resultat is amazing : GRB 990123 was also very bright in optical, peaking at magnitude 8.9 [16]. As the measured redshift was $z = 1.6$ (see later), the same source located at 1 kpc would been as bright as the sun ! Figure 11 shows the three ROTSE images as well as the time profile of GRB 990123.

2.2 Afterglow

2.2.1 Observational strategy

The typical BATSE GRB error box has a radius of a few degrees which makes very difficult the search for any counterpart at other wavelengths. The Beppo-SAX satellite was able to reduce this radius to a few arcminutes when a GRB is detected by the Wide Field Cameras (WFC) in the 2-28 keV

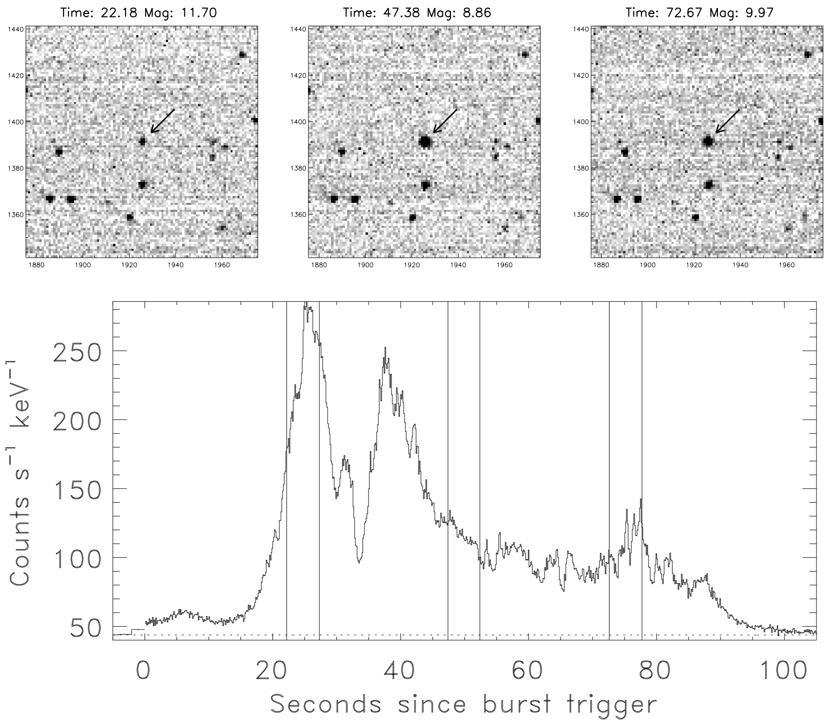

Fig. 11. GRB 990123 : *Upper panel :* the three ROTSE prompt optical images [16]. *Lower panel :* BATSE time profile. The vertical lines correspond to the three optical observations.

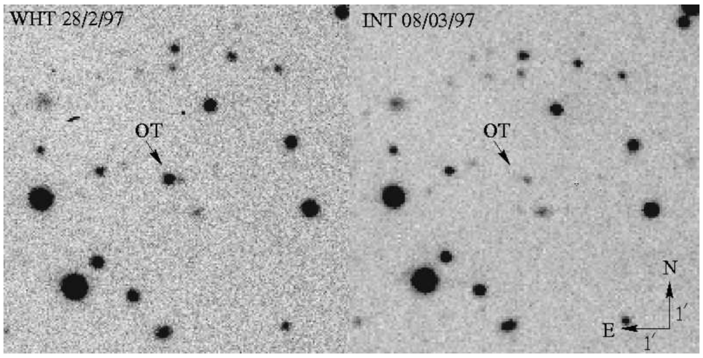

Fig. 12. GRB 970228 afterglow : the fading optical transient (OT) (from [17]).

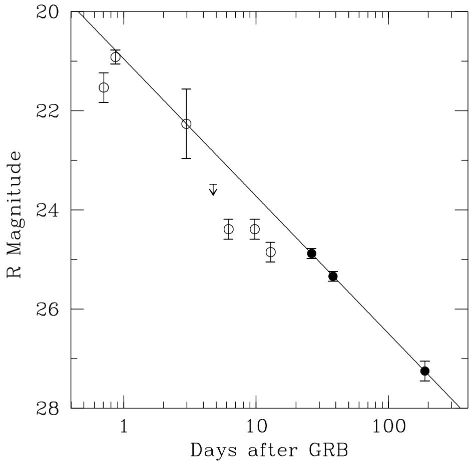

Fig. 13. GRB 970228 afterglow : Evolution of the R band magnitude of the OT during 200 days [18].

band. Once per orbit, Beppo-SAX data were transmitted to the ground so that in case of detection, the GRB position can be distributed to ground-based observatories within a few hours. This observational strategy has allowed in 1997 the first detection of an optical counterpart to a GRB (GRB 970228). This first discovery has been followed by many others[2], in several spectral bands (X-ray, optical and radio bands). The Beppo-SAX mission has ended in April 2002 and GRB alerts are now provided by the HETE-2 satellite, which has been joined by INTEGRAL since October 2002. The SWIFT mission (to be lauched at the end of 2003) will increase the rate of GRB localizations up to about 150 per year.
These couterparts are observed after the end of the prompt gamma-ray emission (typically a few hours after the GRB in the case of the Beppo-SAX detections) and their luminosity is decreasing down to the limit of detection (see figure 12). They are named “afterglows” to distinguish them from the prompt burst emission. An important issue that should be solved in the coming years thanks to HETE-2, INTEGRAL and SWIFT is the understanding of the transition period between the burst and its afterglow.

[2]Jochen Greiner is maintaining a web page with a very useful list of all well located GRBs and their detected afterglows : `http://www.mpe.mpg.de/ jcg/grbgen.html`

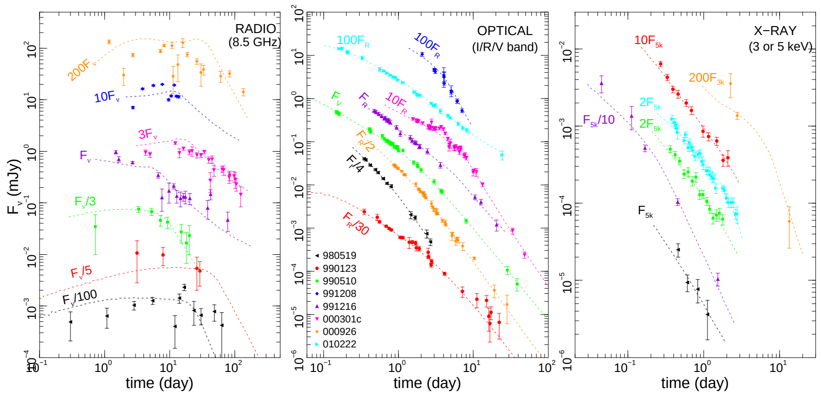

Fig. 14. Radio, optical and X-ray lightcurves of a few GRBs (from [19]).

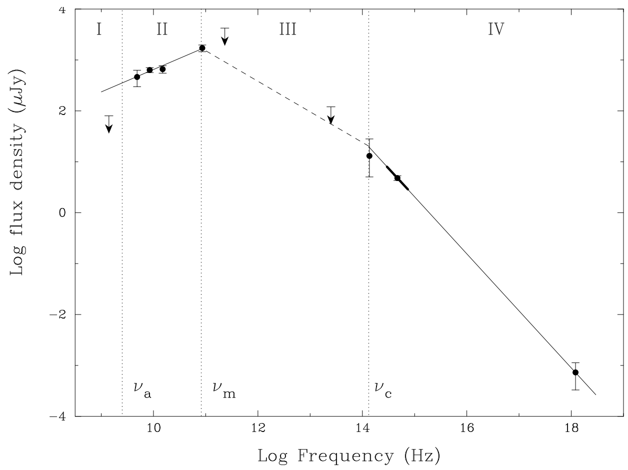

Fig. 15. Spectrum of the afterglow of GRB 970507 at 12 days (from [20]).

2.2.2 Lightcurve and spectrum

In a first approximation, the flux of the afterglow at a given frequency is decreasing as a power-law. For instance, figure 13 shows the lightcurve of the afterglow of GRB 970228 in the R band. In most cases, the lightcurve cannot be represented by a unique power-law but is better discribed as a succession of power-laws with different slopes, separated by one or several breaks (see figure 14). The spectrum is also made of several power-laws with evolving break frequencies (see for instance the spectrum of the afterglow of GRB 970507 after 12 days in figure 15). Then, on a large time interval

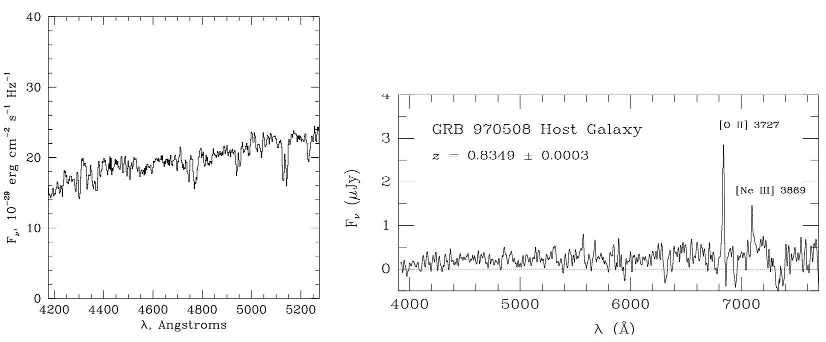

Fig. 16. Redshift of GRB 970508 : *Left* : spectrum of the optical transient, showing FeII and MgII absorption lines at $z = 0.835$ [21] ; *Right* : spectrum of the host galaxy, showing [OII] and [NeIII] emission lines at $z = 0.835$ [22].

and over a broad energy range, the flux of a GRB afterglow is

$$F_\nu(t) \propto \nu^{-\alpha} \times t^{-\beta} \ , \tag{2.7}$$

α and β depending on the spectral range and the period of observation. Typically, the observed β is in the interval 0.6–2.2. We will see in section 4 that this behaviour is very well understood as the synchrotron emission of relativistic electrons accelerated in a strong ultra-relativistic shock, due to the deceleration of a relativistic shell by its environment.

2.2.3 Redshift

The first important consequence of the detection of the optical afterglow is the possibility to take a good-quality spectrum of the object and find lines allowing the determination of the redshift of the source. The first redshift determination occured in the case of the afterglow of GRB 970508 thanks to the presence of several absorption lines in the spectrum of the optical transient (see figure 16, left). It was shown that the most distant absorbing medium was located at $z = 0.835$ [21]. Later, emission lines have been identified at the same redshift in the spectrum of the host galaxy (see figure 16, right), making this redshift determination very reliable [22]. This is of course a very important result, providing the only direct proof of the cosmological origin of (at least long duration) GRBs ! About 25 redshifts have now been obtained directly from the OT and/or from the host galaxy spectrum, with redshifts going from $z \sim 0.36$ (GRB 990712) to $z \sim 4.5$ (GRB 000131) : see table 1. An important consequence of this very distant origin is that the energy released during the GRB is huge : the equivalent isotropic energy computed from the distance (assuming "standard" cosmo-

1997	GRB	970228	970508	970828	971214		
	z	0.695	0.835	0.958	3.42		
1998	GRB	980613	980703				
	z	1.096	0.966				
1999	GRB	990123	990510	990705	990712	991208	991216
	z	1.60	1.619	0.86	0.434	0.706	1.02
2000	GRB	000131	000301C	000418	000911	000926	
	z	4.5	2.03	1.118	1.058	2.066	
2001	GRB	010222	010921	011121	011211		
	z	1.477	0.45	0.36	2.14		
2002	GRB	020405	020813	021004	021211		
	z	0.69	1.25	2.3	1.01		

Table 1. The redshift of GRB afterglows detected from 1997 to 2002 (measured from the OT and/or host galaxy spectrum).

logical parameters) and the observed gamma-ray fluence is

$$E_{\gamma,4\pi} = 4\pi D_{\mathrm{L}}^2(z)\ \frac{\mathcal{F}_\gamma}{1+z} \simeq 10^{51} \to 10^{54}\ \mathrm{erg}\ . \tag{2.8}$$

We will see in section 4 that some of the breaks observed in the afterglow lightcurves are good evidences in favor of a beamed emitting ejecta. Then the values of equation 2.8 have to be multiplied by a factor $\Omega/4\pi$, where Ω is the opening angle of the emitting ejecta. The method for the determination of $\Omega/4\pi$ from the observed break time will be explained in section 4. The result will be to decrease the total gamma-ray energy to about 10^{51} erg, with a large uncertainty. This is still equivalent to the total kinetic energy of a supernova radiated only in the 20 keV – 20 MeV energy range !

2.2.4 Host galaxy

The study of the host galaxies of GRB afterglows is a very interesting emerging topic, as it is a very peculiar sample of distant galaxies, selected with totally unusual methods. Their main properties have been summerized by Djorgoski et al. in a recent review [23] : they are faint ($\langle R\rangle \sim 25$) galaxies at redshift $\langle z\rangle \sim 1$, have a large range of luminosities and morphologies, are broadly typical for the normal, evolving, actively star-forming galaxies at comparable z and R magnitude. There are some evidence of a somewhat elevated SFR per unit luminosity and some spectroscopic hints of massive star formation. The typical observed SFR in these galaxies is about a few $M_\odot$/yr but a high fraction of the total star formation may be obscured by dust.

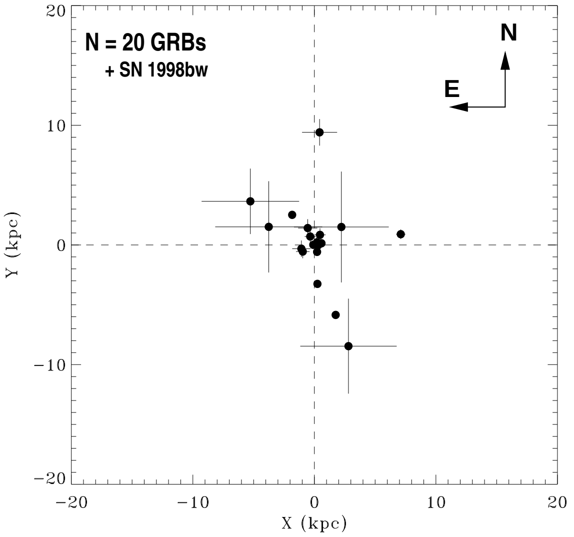

Fig. 17. Position of the optical transient inside its host galaxy (from [24]).

An important question regarding the identification of the GRB progenitors is the location of the GRB inside its host galaxy. We will see in section 6 that the two main families of models are (i) the merger of two compact objects and (ii) the collapse of very massive stars (collapsars). The second case leads to GRBs located in the star-forming region of the host galaxy whereas the first case should produce GRBs distributed at larger distances from the central region of the galaxy, due to a long delay between the binary system formation and the merger. As can be seen in figure 17, the study of the location of the optical transient in its host galaxy seems to favor an association with central star-forming region [24] and then to favor the collapsar model. Of course, this concerns only the long-duration bursts, as no afterglow has ever been detected in association with a short GRB.

2.2.5 Other aspects

We list here a few observational facts that have not been developped elsewhere in this section.

The supernova connection In several classes of models, GRBs are associated with a supernova, exploding either before or simultaneously to the GRB. There are a few observationnal evidences in favor of such an association : (i) a type Ic supernova (SN 1998bw) has been found in the error box of GRB 980425 [20]. The analysis of the lightcurve and spectrum of this supernova shows that it is a very energetic one, with probably an ejected

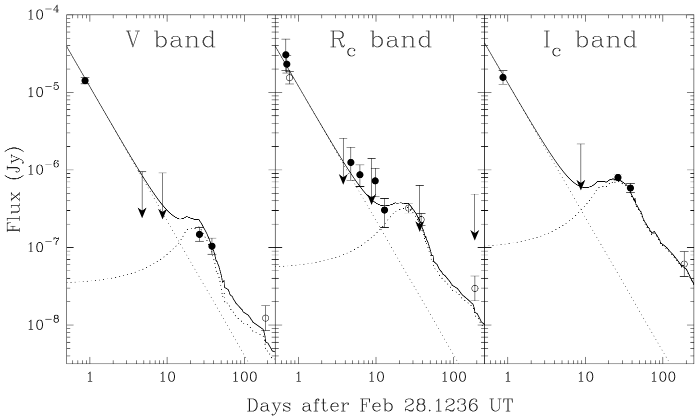

Fig. 18. Lightcurve of the optical afterglow of GRB 970228 (from [26]).

enveloppe which was initially midly relativistic. The main question regarding the SN1998bw-GRB 980425 association is that it leads to a very low redshift as SN1998bw is located at $z = 0.0085$. As GRB 980425 has gamma-ray properties which are absolutely normal (based on the properties of the more than 2500 BATSE GRBs), especially concerning the peak energy and the fluence, it implies that GRB 980425 is a very peculiar underluminous gammma-ray burst, with an equivalent isotropic energy many orders of magnitude below the usual values (10^{51}–10^{54} erg) ; (ii) a SN lightcurve could be hiden behind the afterglow lightcurve and appear at late time as a small "bump". Such bumps have been observed in several cases (see figure 18) when the afterglow is very faint. However, it seems that there are other interpretations which are not related to a supernova but for instance to inhomogeneities in the external medium or to a late heating from decaying neutrons [25].

Lines in the X-ray afterglow ? Evidence for spectral lines have been found in a few X-ray afterglows. See for instance the Chandra spectrum of the X-ray afterglow of GRB 991216 in figure 19 and the XMM-Newton spectrum of the X-ray afterglow of GRB 011211 in figure 20. Should these lines be confirmed, they would provide strong constraints on GRB models, especially on the initial event responsible for the burst. They would indeed show that the close environment of the source is very metal rich, as for instance in a supernova remnant, enforcing the possible supernova-gamma ray burst connection.

The afterglow polarization Polarization has been measured in a few optical afterglows, typically at one day after the burst, showing a linear polarization of a few percents [29,30]. The interpretation of this polarization, which is evolving in time is not very simple but seems to be in agreement

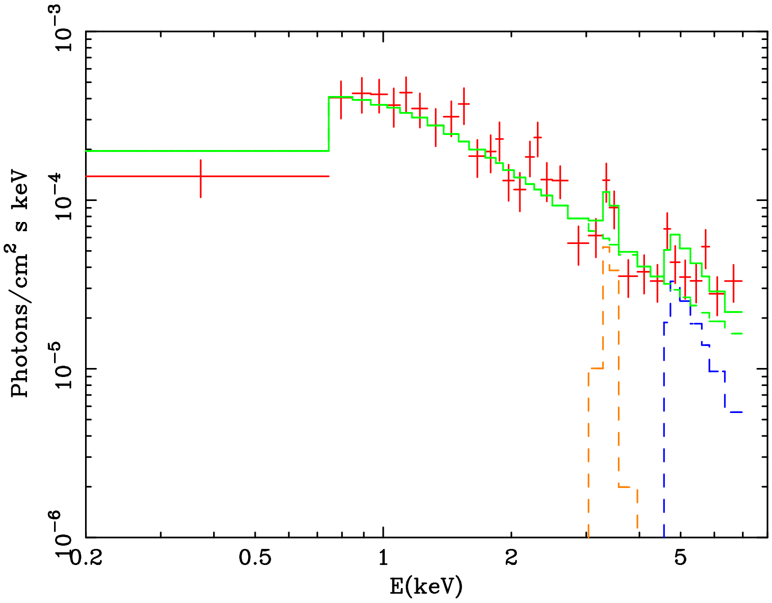

Fig. 19. Chandra observation of GRB 991216 (from [27]).

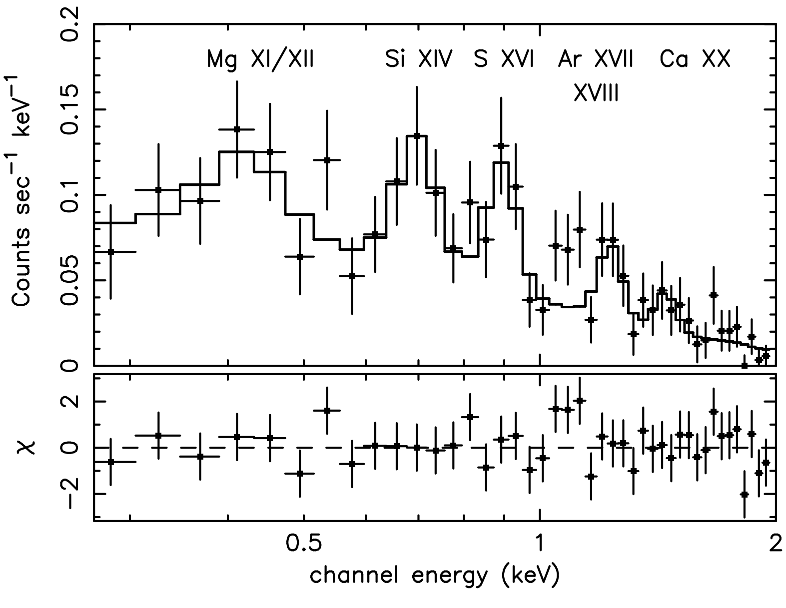

Fig. 20. XMM-Newton observation of GRB 011211 (from [28]).

with the general picture (described in section 4) of an afterglow produced by the synchrotron radiation of a beamed relativistic ejecta (see e.g. [31]).

3 Theoretical scenario

In this section, we describe the key arguments leading to the most discussed theoretical scenario for cosmological GRBs.

3.1 Distance scale

In this lecture, we will only consider the case of GRBs produced at cosmological distances. We know from the redshift measurements in about 25 afterglows (see section 2) that this is certainly the case for a large fraction of the long duration GRBs ($T_{90} \gtrsim 2$ s). The isotropic distribution over the sky of the GRBs detected by BATSE (figure 1) as well as the observed value of the $\langle V/V_{\rm max}\rangle$ indicator,

$$\left\langle \frac{V}{V_{\rm max}} \right\rangle \simeq 0.328 \pm 0.012 \text{ (first 601 BATSE GRBs)} , \qquad (3.1)$$

clearly smaller than the 0.5 value corresponding to a homogeneous distribution in a Euclidian space, are clearly strong evidences that most GRBs if not all (short and long duration bursts) are indeed produced at large redshifts. Then all acceptable models of GRBs must consider extragalactic sources. An important issue is of course the distribution of GRBs with redshift, as it can put some constraints on their progenitors. It would in particular be very important to know if the rate of GRBs (or at least of a sub-group of GRBs, especially the long ones) is following the star formation rate (SFR). The number of redshift measurements (~ 25) is still too low to be able to construct directly this rate. The SWIFT mission will increase the number of afterglow detection and should greatly improve the present situation, where the information has to be extracted from other data. The most useful tool is the $\log N$–$\log P$ diagram, where the number N of GRBs with a peak flux larger that P is plotted as a function of P (see figure 21). The method consists in fitting this curve by assuming a GRB rate, a GRB luminosity function and the "standard" values for the cosmological parameters. The main problem is that it is impossible to discriminate between models as different as a GRB rate constant in time or proportional to the SFR. In figure 21, we show an example of a fit obtained in the last case (the GRB rate follows the SFR), which is the situation expected in the collapsar model where the GRB progenitors are massive stars. The rate with is obtained is about one GRB for 10^6 type II supernovae [32]. This estimate of course assumes an isotropic emission. As the emission is more probably beamed with an opening angle Ω, this rate has to be multiplied by a factor $(\Omega/4\pi)^{-1}$ which could be of the order of 500-1000 according to recent estimates [33].

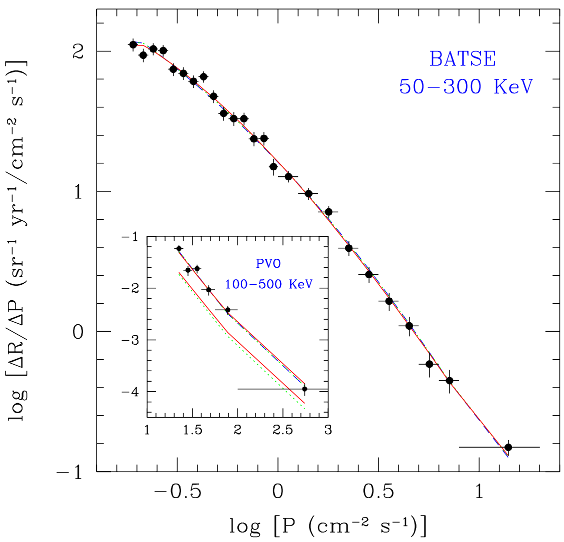

Fig. 21. The $\log N$–$\log P$ diagram of BATSE GRBs (some untriggered bursts being included [34]) and the fit obtained assuming that the GRB rate follows the star formation rate [32].

3.2 Compact source – Relativistic motion

After the distance scale, the second key ingredient in every realistic model is to assume that the source of radiation is compact but relativistically moving. The basic argument is very simple : as we have seen in section 2, the energy radiated in gamma-rays by a GRB is

$$E_\gamma \geq f_\Omega\ 10^{51}\ \mathrm{erg}\ , \tag{3.2}$$

where $f_\Omega = \Omega/4\pi$ and Ω is the opening angle of the emitting source. On the other hand, the rapid variability observed in the GRB time profiles down to timescales

$$t_{\mathrm{var}} \leq 10\ \mathrm{ms} \tag{3.3}$$

implies that the source of radiation is compact with a typical size

$$R \leq c t_{\mathrm{var}} \leq 3000\ \mathrm{km}\ . \tag{3.4}$$

It is then easy to estimate the corresponding opacity $\tau_{\gamma\gamma}$ to pair production ($\gamma\gamma \to e^+e^-$) :

$$\tau_{\gamma\gamma} \simeq \frac{f_{\gamma\gamma} E_\gamma \sigma_{\mathrm{T}}}{4\pi R^2 m_{\mathrm{e}} c^2} \geq 7\ 10^{14}\ f_\Omega\ f_{\gamma\gamma}\ , \tag{3.5}$$

where $f_{\gamma\gamma}$ is the fraction of the gamma-ray photons above the pair production threshold (see e.g. [35]). As most GRB spectra have a large fraction of high-energy gamma-ray photons and as current estimates of f_Ω are of the order of 10^{-2}–10^{-3}, it is impossible to avoid very large values of the optical depth $\tau_{\gamma\gamma}$. Then the number of pairs produced in the source should increase very rapidly, resulting in a very large optical depth for all photons. However, the non-thermal nature of GRB spectra indicate that the sources are certainly optically thin. This so-called "compactness problem" can be easily solved if the emitting material is assumed to be moving relativistically. If the emitting matter moves with a large Lorentz factor $\Gamma = 1/\sqrt{1-v^2/c^2}$, then two effects will reduce dramatically the optically depth $\tau_{\gamma\gamma}$: (i) the photon energies in the comoving frame of the source are reduced by a factor $\sim \Gamma$, resulting in a much softer spectrum (typically peaking in the X-ray domain for $\Gamma \sim 100$) where the fraction $f_{\gamma\gamma}$ of high-energy photons above the pair production threshold is much lower. If the observed high energy spectral index is β ($\beta \sim -2.25$), $f_{\gamma\gamma}$ is divided by $\sim \Gamma^{-2\beta-2}$. (ii) the size of the emitting region allowed to produce variability on a time scale $t_{\rm var}$ is multiplied by $\sim \Gamma^2$ (see section 5), leading to

$$R \lesssim \Gamma^2 c t_{\rm var} = \left(\frac{\Gamma}{100}\right)^2 \ 3\ 10^7\ \mathrm{km}\ . \tag{3.6}$$

Then the new optical depth for pair production in the relativistically moving case is

$$\tau_{\gamma\gamma} \simeq \frac{\Gamma^{2\beta+2}\ f_{\gamma\gamma} E_\gamma \sigma_{\rm T}}{4\pi\Gamma^4 R^2 m_{\rm e} c^2} \geq 7\ 10^{14}\ f_\Omega\ f_{\gamma\gamma}\ \Gamma^{-(2-2\beta)}\ . \tag{3.7}$$

It is clear that for

$$\Gamma \gtrsim \left(7\ 10^{14}\ f_\Omega\ f_{\gamma\gamma}\right)^{\frac{1}{2-2\beta}} \simeq 200\ \left(f_\Omega f_{\gamma\gamma}\right)^{0.15}\ \text{ for } \beta = -2.25, \tag{3.8}$$

the optical depth $\tau_{\gamma\gamma}$ is smaller than unity. Recently, precise determinations of the minimum Lorentz factor required to garanty an optically thin source have been obtained for a few GRBs for which the redshift z was known (allowing a precise estimate of E_γ) and for which a good-quality high-energy spectrum was available (allowing a precise estimate of $f_{\gamma\gamma}$). The authors have considered not only the pair production process but also the scattering of photons by the pair-created electrons and positrons and the scattering of photons by the ambient electrons (accompanying the baryons). They find Lorentz factors in the interval 24-420, most minimum values being above 100 [36]. This indicates that GRBs are associated to the most relativistic flows known in the Universe (micro-quasars or blazars having Lorentz factors of a few tens only).

3.3 Fireballs

The last argument leads to the concept of fireball, which is used in the most discussed models of GRBs, even if this is not exactly with the same definition that was first introduced by Paczyński [37] and Goodman [38]. Assume that a large amount of energy E is released in a small spherical volume of radius R_0. Whatever the dominant form of this energy (photons, electrons/positrons, magnetic energy, ...) is, the medium is initially completely optically thick (see previous subsection) and will first follow a purely adiabatic spherical expansion in the ambient medium, during which part of the internal energy will be converted into kinetic energy. The special relativistic equations of hydrodynamics in one dimension and spherical symmetry are (with $c = 1$)

$$\frac{\partial D}{\partial t} + \frac{1}{R^2}\frac{\partial}{\partial R}\left(R^2 D v\right) = 0 \text{ (mass conservation) ,} \quad (3.9)$$

$$\frac{\partial S}{\partial t} + \frac{1}{R^2}\frac{\partial}{\partial R}\left(R^2 S v\right) = -\frac{\partial P}{\partial R} \text{ (momentum conservation) ,} \quad (3.10)$$

$$\frac{\partial \tau}{\partial t} + \frac{1}{R^2}\left(R^2(\tau + P)v\right) = 0 \text{ (energy conservation ,} \quad (3.11)$$

where t and R are the time and the radius in a fixed frame linked to the central source, D, S and τ are the mass, momentum and energy density (the rest-mass energy being substracted) in the frame frame. These quantities are related to the velocity v, the Lorentz factor $\Gamma = 1/\sqrt{1-v^2}$ and comoving quantities by

$$D = \rho\Gamma \ , \quad (3.12)$$

$$S = \rho h \Gamma^2 v \ , \quad (3.13)$$

$$\tau = \rho h \Gamma^2 - P - D \ , \quad (3.14)$$

where ρ is the mass density, P is the pressure, $h = 1 + \epsilon + P/\rho$ the specific enthalpy and ϵ the specific energy in the comoving frame. If the medium behaves as a perfect fluid of adiabatic index γ, we have

$$\epsilon = \frac{1}{\gamma - 1}\frac{P}{\rho} \ . \quad (3.15)$$

In this case, the last equation (energy conservation) can be rewritten as

$$\frac{\partial}{\partial t}\left(P^{\frac{1}{\gamma}}\Gamma\right) + \frac{1}{R^2}\left(R^2 P^{\frac{1}{\gamma}}\Gamma v\right) = 0 \ . \quad (3.16)$$

In our context, it is very useful to use a new set of coordinates, where t is replaced by the "arrival time" $t_{\mathrm{a}} = t - R/c$, which is the time at which photons emitted at time t and radius R are detected by an observer located at distance D from the source, fixing the origin of time at the arrival time of photons emitted by the source ($R=0$) at $t=0$. The equations become

$$\frac{1}{R^2}\frac{\partial}{\partial R}\left(R^2\rho\Gamma v\right) = -\frac{\partial}{\partial t_{\mathrm{a}}}\left(\rho\Gamma(1-v)\right) , \quad (3.17)$$

$$\frac{1}{R^2}\frac{\partial}{\partial R}\left(R^2\left(\rho h\Gamma^2 v^2\right)\right) = -\frac{\partial}{\partial t_{\mathrm{a}}}\left(\rho h\Gamma^2 v(1-v)\right)+\frac{\partial P}{\partial t_{\mathrm{a}}}-\frac{\partial P}{\partial R} , \quad (3.18)$$

$$\frac{1}{R^2}\frac{\partial}{\partial R}\left(R^2 P^{\frac{1}{\gamma}}\Gamma v\right) = -\frac{\partial}{\partial t_{\mathrm{a}}}\left(P^{\frac{1}{\gamma}}\Gamma(1-v)\right) . \quad (3.19)$$

If $\Gamma \gg 1$, the velocity becomes very close to the speed of light, with

$$1-v \simeq \frac{1}{2\Gamma^2} . \quad (3.20)$$

It is then easy to show that all terms in the right hand side of the three equations above are negligible for small radii compared to the left hand side terms. This leads to three conservation equations :

$$R^2\rho\Gamma \simeq \text{constant} , \quad (3.21)$$

$$R^2\rho h\Gamma^2 \simeq \text{constant} , \quad (3.22)$$

$$R^2 P^{\frac{1}{\gamma}}\Gamma \simeq \text{constant} . \quad (3.23)$$

These equations are valid for each shells of the relativistic ejecta, that evolve independently in this regime, as these equations are now only R dependent. This approximation breaks at the spreading radius that is defined in equation 3.35 below. A general solution to this system of three equations is (see e.g. [35]) :

$$\left(\frac{R}{R_0};\frac{\rho}{\rho_0};\frac{P}{P_0}\right) = f\left[\gamma;\frac{\Gamma_\infty}{\Gamma_0};\quad\frac{\Gamma}{\Gamma_0}\right] , \quad (3.24)$$

with

$$\frac{R}{R_0} = \left(\frac{\Gamma_\infty}{\Gamma_0}-1\right)^{\frac{1}{2(\gamma-1)}}\left(\frac{\Gamma_\infty}{\Gamma}-1\right)^{-\frac{1}{2(\gamma-1)}}\left(\frac{\Gamma}{\Gamma_0}\right)^{-1/2} , \quad (3.25)$$

$$\frac{\rho}{\rho_0} = \left(\frac{\Gamma_\infty}{\Gamma_0}-1\right)^{-\frac{1}{\gamma-1}}\left(\frac{\Gamma_\infty}{\Gamma}-1\right)^{\frac{1}{\gamma-1}} , \quad (3.26)$$

$$\frac{P}{P_0} = \left(\frac{\Gamma_\infty}{\Gamma_0}-1\right)^{-\frac{\gamma}{\gamma-1}}\left(\frac{\Gamma_\infty}{\Gamma}-1\right)^{\frac{\gamma}{\gamma-1}} , \quad (3.27)$$

where R_0, ρ_0, P_0 and Γ_0 are the initial values of R, ρ, P and Γ when the relativistic expansion starts and Γ_∞ is given by

$$\Gamma_\infty = h_0\Gamma_0 \text{ with } h_0 = 1+\frac{\gamma}{\gamma-1}\frac{P_0}{\rho_0} . \quad (3.28)$$

The ejecta experiences successively two phases :

- **The radiation dominated phase :** the internal energy term dominates in the specific enthalpy so that (the adiabatic index γ is of course extremely close to 4/3 is this phase) :

$$\frac{\Gamma}{\Gamma_0} \simeq \frac{R}{R_0}\ , \tag{3.29}$$

$$\frac{\rho}{\rho_0} \simeq \left(\frac{R}{R_0}\right)^{-3}\ , \tag{3.30}$$

$$\frac{P}{P_0} \simeq \left(\frac{R}{R_0}\right)^{-4}\ . \tag{3.31}$$

As $\Gamma \propto R$ and $P/\rho \propto R^{-1}$, this is clearly an acceleration phase where the internal energy is converted into kinetic energy.

- **The matter dominated phase :** the rest-mass energy term now dominates in the specific enthalpy so that

$$\Gamma \simeq \Gamma_\infty\ , \tag{3.32}$$

$$\frac{\rho}{\rho_0} \simeq \left(\frac{R}{R_0}\right)^{-2}\ , \tag{3.33}$$

$$\frac{P}{P_0} \simeq \left(\frac{R}{R_0}\right)^{-2\gamma}\ . \tag{3.34}$$

In this phase, the Lorentz factor has reached its terminal value Γ_∞ and is constant. It is possible to show that the width Δ of the ejecta remains constant up to the spreading radius

$$R_{\mathrm{spreading}} \simeq \frac{\Gamma_\infty^2}{\Gamma_0}\Delta \simeq 4.8\ 10^{16}\ \Gamma_0\ \left(\frac{\Gamma_\infty/\Gamma_0}{400}\right)^2 \left(\frac{\Delta/c}{10\ \mathrm{s}}\right)\ \mathrm{cm}\ . \tag{3.35}$$

At the spreading radius, the approximation corresponding to equations 3.21–3.23 is not valid anymore and the complete hydrodynamics equations have to be considered.

The transition between the two phases occurs at the saturation radius R_{sat} where Γ reaches the terminal value Γ_∞, i.e.

$$R_{\mathrm{sat}} \simeq R_0\frac{\Gamma_\infty}{\Gamma_0} \simeq 1.2\ 10^9\ \left(\frac{\Gamma_\infty/\Gamma_0}{400}\right)\ \mathrm{cm}\ . \tag{3.36}$$

The complete solution for $\gamma = 4/3$ and $\Gamma_\infty/\Gamma_0 = 400$ is plotted in figure 22. The energy fluxes are given by

$$\dot{E} = \dot{E}_{\mathrm{kin}} + \dot{E}_{int}\ , \tag{3.37}$$

$$\dot{E} = 4\pi R^2 \rho h \Gamma^2 c = \Gamma_\infty \dot{M} c^2 = \text{constant (total energy flux)}\ , \tag{3.38}$$

$$\dot{M} = 4\pi R^2 \rho \Gamma c = \text{constant (mass flux)}\ . \tag{3.39}$$

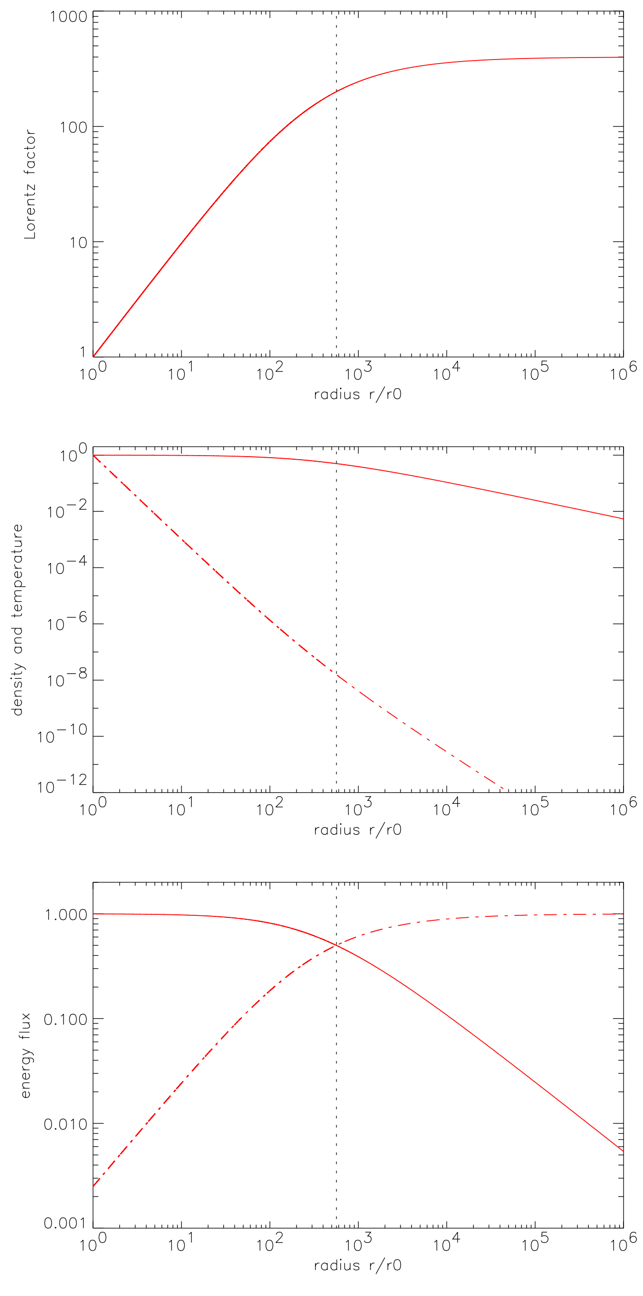

Fig. 22. The fireball adiabatic evolution for $\Gamma_\infty/\Gamma_0 = 400$. The dotted vertical line indicates the saturation radius $R_{\rm sat}$. First panel : evolution of the Lorentz factor. Second panel : evolution of the comoving density (dashed line) and the temperature in the observer frame (solid line). Third panel : evolution of the kinetic (dashed line) and internal (solid line) energy fluxes (the sum being constant).

The kinetic and internal energy fluxes $\dot{E}_{\rm kin}$ and $\dot{E}_{\rm int}$ plotted in figure 22 are given by

$$\begin{aligned} \dot{E}_{\rm kin} &= \Gamma \dot{M} c^2 = \frac{\Gamma}{\Gamma_\infty} \dot{E} \ , & (3.40) \\ \dot{E}_{\rm int} &= \left(\Gamma_\infty - \Gamma\right) \dot{M} c^2 = \left(1 - \frac{\Gamma}{\Gamma_\infty}\right) \dot{E} \ . & (3.41) \end{aligned}$$

The temperature in the observer frame is $T = \Gamma T'$ where the comoving temperature is $T' = \left(3P/a\right)^{1/4}$. Then

$$\begin{aligned} \frac{T}{T_0} &= \left(\frac{\Gamma_\infty}{\Gamma_0} - 1\right)^{-1} \left(\frac{\Gamma_\infty}{\Gamma} - 1\right) \left(\frac{\Gamma}{\Gamma_0}\right) \ , & (3.42) \\ &\simeq 1 \text{ (radiation dominated phase) } , & (3.43) \\ &\simeq \left(\frac{R}{R_0}\right)^{-1} \text{ (matter dominated phase) } . & (3.44) \end{aligned}$$

The initial temperature of the fireball is related to the released energy by

$$kT_0 \simeq 1.1\ \Gamma_0^{1/2} \left(1 - \frac{\Gamma_0}{\Gamma_\infty}\right)^{1/4} \left(\frac{\dot{E}}{10^{51}\ \mathrm{erg/s}}\right)^{1/4} \left(\frac{R_0}{30\ \mathrm{km}}\right)^{-1/2} \mathrm{MeV}\ . \tag{3.45}$$

It can be shown that the optical depth for pair creation falls below unity when the comoving temperature T' drops below $T'_{\rm pairs} \sim 20$ keV. This uusally occurs in the radiation dominated phase, at radius (see e.g. [35])

$$R_{\rm pairs} \simeq 1.7\ 10^8\ \Gamma_0^{-1/2} \left(\frac{\dot{E}}{10^{51}\ \mathrm{erg/s}}\right)^{1/4} \left(\frac{R_0}{30\ \mathrm{km}}\right)^{1/2} \left(\frac{T'_{\rm pairs}}{20\ \mathrm{keV}}\right)^{-1} \mathrm{cm}\ . \tag{3.46}$$

In the initial version of the fireball model, the ejecta was assumed to be purely leptonic and all the energy was radiated at this stage to produce the GRB. The predicted spectrum was of course thermal, which is in contradiction with the observations. For this reason, it is now assumed that there is a small baryonic pollution in the initial stage of energy release. Then the fireball remains optically thick up to the beginning of the matter-dominated phase, mainly due to the scattering of photons by the electrons accompanying the baryons. These bayons of course dominate the mass flux $\dot{M}$. As the terminal Lorentz factor is given by $\Gamma_\infty/\Gamma_0 = \dot{E}/\dot{M}c^2$, the baryonic load must remain at a very low level ($\dot{M}c^2/\dot{E} < 10^{-2}$) to reach the Lorentz factors that are required ($\Gamma_\infty > 100$, see previous subsection). This is not easy to obtain and puts a severe constraint on models for the GRB central engine (see section 6).

In the matter-dominated phase ($\Gamma \simeq \Gamma_\infty$ and $\rho \propto R^{-2}$), photons emitted at radius R inside the relativistic ejecta will escape at radius $R_{\rm esc}(R) \simeq R+2\Gamma^2\Delta$. Then the Thomson optical depth at radius R is given by (see [39] for a complete derivation) :

$$\tau(R) \simeq \int_R^{R_{\rm esc}(R)} \frac{\sigma_{\rm T}\rho}{m_{\rm p}}\frac{dr}{2\Gamma} \simeq \frac{\sigma_{\rm T}\rho_0 R_0 \Gamma_0}{2\Gamma_\infty^2 m_{\rm p}}\frac{R_0}{R}\frac{2\Gamma_\infty\Delta}{R+2\Gamma_\infty\Delta}\ . \tag{3.47}$$

For usual GRB parameters $R \ll 2\Gamma_\infty^2\Delta$ when the fireball becomes optically thin, and then the photospheric radius $R_{\rm ph}$ is given by

$$R_{\rm ph} \simeq 9.2\ 10^9\ \Gamma_0^{-3}\left(\frac{\dot{E}}{10^{51}\ \mathrm{erg/s}}\right)\left(\frac{\Gamma_\infty/\Gamma_0}{400}\right)^{-3}\ \mathrm{cm}\ . \tag{3.48}$$

As the acceleration is essentially completed well before this radius, the remaining internal energy that can be radiated at the photosphere is small. It can however produce a thermal precursor to the GRB which will be discussed in section 5.

In conclusion, the baryonic loaded fireball provides a natural way to convert the initial energy realeased into a highly relativistic ejecta that becomes optically thin at large distance from the source, where new processes can operate to convert a fraction of the kinetic energy into radiation (with an optically thin spectrum) and produce the GRB and its afterglow.

3.4 A three-step scenario

All these considerations lead to a three-step theoretical scenario for GRBs:

1. Central engine : an initial event is responsible for a huge energy release. This energy is first injected into a highly relativistic ejecta. This step is probably the less understood today and will be discussed in section 6.
2. Production of the prompt emission : at large distance from the source, the relativistic ejecta becomes transparent and can radiate part of its kinetic energy to produce the GRB. Several mechanisms have been proposed. We will discuss in section 5 the most popular one : the "internal shock" model.
3. Production of the afterglow : at even larger radii, the deceleration of the relativistic ejecta by the surrounding medium becomes important. If the remaining kinetic energy after the second step is still high, a strong shock appears (the so-called "external shock") and propagates within the external medium. The electrons accelerated behind this strong shock radiate and produce the observed afterglow. This will be described in section 4.

Central engine (see section 6)	R_0	10^6-10^7 cm	Initial energy release → baryonic loaded ejecta → becomes relativistic
	R_{sat}	10^8-10^{10} cm	End of the acceleration $\rightarrow \Gamma \sim \Gamma_\infty \geq 100$
Prompt emission (see section 5)	R_{ph}	10^{10}-10^{12} cm	Transparency → thermal precursor ?
	R_{GRB}		Kinetic energy → radiation → prompt GRB
Afterglow (see section 4)	R_{dec}	10^{13}-10^{18} cm	Deceleration starts → "external shock" → afterglow

Table 2. The three-step theoretical scenario for cosmological gamma-ray bursts.

This three-step scenario apply to most GRB models, which usually have in common the last step (which is the most constrained by the observations) and differ in the second or in the first step. Notice that the deceleration radius at which the third step starts can be easily estimated (see section 4). For a uniform medium of density n it is given by

$$R_{\mathrm{dec}} \simeq 4.6\ 10^{16} \left(\frac{E}{10^{53}\ \mathrm{erg}}\right)^{1/3} \left(\frac{n}{1\ \mathrm{cm}^{-3}}\right)^{-1/3} \left(\frac{\Gamma_\infty}{400}\right)^{-2/3}\ \mathrm{cm}\ . \quad (3.49)$$

Table 2 presents a summary of this scenario with all important radii.

4 Afterglow

In this section, we describe the production of the afterglow. We assume that a source has produced a highly relativistic ejecta and that after the gamma-ray burst has been produced, the mean Lorentz factor is Γ_0 and the equivalent isotropic kinetic energy is E_0.

4.1 The external shock

At large radii, when the swept-up mass becomes large, the relativistic ejecta is decelerated by the external medium. Two shocks are formed : (i) a forward shock (the so-called "external shock"), which propagates within the external medium and (ii) a reverse shock which propagates backwards in the relativistic ejecta. The model where the forward shock is responsible for the afterglow works very well [40] and will be detailed below. The emission associated with the reverse shock is not so well understood and is still largely debated. It will be discussed in section 5.

A key ingredient of afterglow models is the assumption about the density profile of the external medium. In particular, mergers of compact object should occur in low density media as they are located far from the central regions of the galaxy, whereas collapsars should have a high density environment (they occur in star-forming regions), possibly dominated by the dense wind of the massive star in its late stages. Therefore the density profile is assumed to be

$$\rho(r) = \frac{A}{r^s} \ , \tag{4.1}$$

with $s = 0$ (uniform medium) and $A = nm_{\rm p}$, where the density n is of order 10^{-3}–$10\ \mathrm{cm}^{-3}$ for mergers and 1–$10^3\ \mathrm{cm}^{-3}$ for collapsars. In the last case, if a dense wind is present, parameters become $s = 2$ and $A = \dot{m}/4\pi v_\infty$ where typical values for a Wolf-Rayet star are a mass loss rate $\dot{m} \simeq 3\ 10^{-5}\ \mathrm{M}_\odot/\mathrm{yr}$ and a terminal velocity $v_\infty \simeq 2000$ km/s, so that $A \simeq 7.6\ 10^{11}\ \mathrm{g.cm}^{-1}$. With such a density profile, the swept-up mass when the relativistic ejecta has reached radius R is

$$M_{\rm ext}(R) = \int_0^R 4\pi r^2 \rho(r) dr = \frac{4\pi}{3-s} A R^{3-s} \ . \tag{4.2}$$

The dynamics of the external shock is described by the self-similar solution of Blandford & McKee [41], which is the relativistic counterpart of the well-known self-similar Sedov solution that applies for supernova remnants. We describe here the main properties of the solution. Assume that the relativistic ejecta initially has a Lorentz factor Γ_0 and a mass $M_0 = E_0/\Gamma_0 c^2$. The deceleration starts when the swept-up mass becomes of the order of M_0/Γ_0. This yields a simple estimate of the deceleration radius :

$$R_{\rm dec} \simeq \left(\frac{3-s}{4\pi}\frac{M_0}{A\Gamma_0}\right)^{\frac{1}{3-s}} \ , \tag{4.3}$$

corresponding for a uniform medium ($s = 0$) of density n to :

$$R_{\rm dec} \simeq 4.6\ 10^{16}\ \left(\frac{E}{10^{53}\ \mathrm{erg}}\right)^{1/3} \left(\frac{n}{1\ \mathrm{cm}^{-3}}\right)^{-1/3} \left(\frac{\Gamma}{400}\right)^{-2/3}\ \mathrm{cm} \tag{4.4}$$

and for a dense stellar wind ($s = 2$) to :

$$R_{\rm dec} \simeq 7.3\ 10^{13}\ \left(\frac{E}{10^{53}\ \mathrm{erg}}\right) \left(\frac{A}{7.6\ 10^{11}\ \mathrm{g.cm}^{-1}}\right)^{-1} \left(\frac{\Gamma}{400}\right)^{-2}\ \mathrm{cm}\ . \tag{4.5}$$

In the ultra-relativistic limit of a strong shock, the comoving density ρ_*, the comoving specific internal energy density ϵ_* in the shocked external medium and the Lorentz factor $\Gamma_{\rm shock}$ of the forward shock are given as a function of the external density $\rho = \rho(R)$ and the Lorentz factor $\Gamma = \Gamma(R)$ of the ejecta at radius $R \geq R_{\rm dec}$ by :

$$\begin{aligned} \rho_* &\simeq (4\Gamma+3)\,\rho \simeq 4\Gamma\rho\ , && (4.6)\\ \epsilon_* &\simeq (\Gamma-1)\,c^2 \simeq \Gamma c^2\ , && (4.7)\\ \Gamma_{\rm shock} &\simeq \sqrt{\frac{(\Gamma+1)(4\Gamma-1)^2}{(8\Gamma+10)}} \simeq \sqrt{2}\Gamma\ . && (4.8) \end{aligned}$$

Equation 4.7 shows that initially (when $\Gamma \gtrsim 100$), the internal energy in the shocked material can be as high as $\sim$ 100 GeV per proton ! Energy conservation combined with these shock conditions leads to :

$$\Gamma_0 M_0 c^2 + M_{\rm ext}(R)c^2 \simeq \Gamma(R) M_0 c^2 + \Gamma^2(R) M_{\rm ext}(R) c^2\ . \qquad (4.9)$$

With the expression of $M_{\rm ext}(R)$ given in equation 4.2, we get the following approximation of the Blandford-McKee solution (see e.g. [42]) :

$$\Gamma(x) \simeq \Gamma_0 \frac{\sqrt{1+4x^{3-s}+\left(2x^{3-s}/\Gamma_0\right)^2}-1}{2x^{3-s}} \text{ with } x = R/R_{\rm dec}\ . \qquad (4.10)$$

We can distinguish three regimes : (i) $R \ll R_{\rm dec}$ ($x \ll 1$) and $\Gamma(R) \simeq \Gamma_0$ (deceleration has not started) ; (ii) $R_{\rm dec} \ll R \ll R_{\rm Sedov}$ ($1 \ll x \ll x_{\rm Sedov}$) and $\Gamma(R) \propto \Gamma_0\,(R/R_{\rm dec})^{-(3-s)/2}$ (deceleration phase) ; (iii) $R \gg R_{\rm Sedov}$ ($x \gg x_{\rm Sedov}$) and $\Gamma(R) \simeq 1$ and $v(R) \propto R^{-(3-s)/2}$ (non-relativistic Sedov phase). The transition to the Sedov phase occur for

$$\frac{R_{\rm Sedov}}{R_{\rm dec}} = x_{\rm Sedov} \simeq \left(\frac{\Gamma_0^2}{3}\right)^{\frac{1}{3-s}}\ . \qquad (4.11)$$

This solution has been plotted in figure 23 for $s=0$ and $n = 1\ \mathrm{cm}^{-3}$ (left) and $s=2$, $\dot{m} = 3\ 10^{-5}\ \mathrm{M}_\odot/\mathrm{yr}$ and $v_\infty = 2000$ km/s (right). The relativistic ejecta parameters are $\Gamma_0 = 400$, $E_0 = 10^{53}$ erg and $M_0 = E_0/\Gamma_0 c^2 = 1.4\ 10^{-4}\ \mathrm{M}_\odot$ in both cases. It is clear that deceleration starts much earlier in the dense wind case. But due to the $\rho \propto r^{-2}$ density profile, the efficiency of the deceleration decreases rapidly and the transition to the non relativistic phase ($\Gamma \sim 1$) occurs approximatively at the same radius in both cases. This shows that only early observations of the afterglow can be used to distinguish between different possible environments. The arrival time $t_{\rm a}$ of afterglow photons emitted when the shock is at radius R has been indicated on the same figure. It is given by

$$t_{\rm a} = t - \frac{R}{c} = \frac{1}{c}\left(\int_0^R \frac{dr}{v/c} - R\right)\ . \qquad (4.12)$$

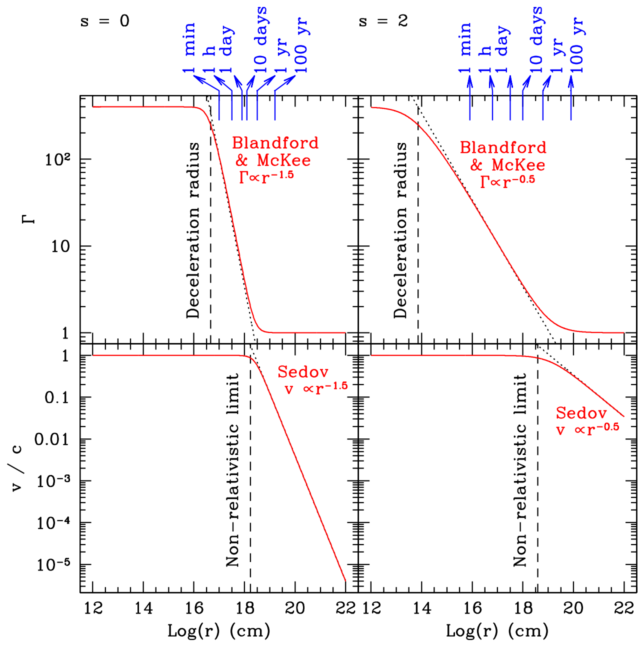

Fig. 23. Lorentz factor and velocity of the external shock as a function of radius for a uniform medium (left) and a non uniform medium with $s = 2$ (right).

4.2 Radiative processes

Physical conditions in the shocked external medium : once the dynamics of the forward shock has been specified, one needs to estimate the distribution of the electrons as well as the magnetic field in the shocked external medium. We assume that a fraction α_{B} of the internal energy density $\rho_* \epsilon_*$ created behind the shock wave is converted into magnetic energy :

$$\frac{B^2}{8\pi} \simeq \alpha_{\mathrm{B}}\ \frac{4\Gamma A}{R^s}\ \Gamma c^2 \tag{4.13}$$

(from eqs. 4.1, 4.6 and 4.7), so that the local field is amplified up to :

$$B \simeq 4\Gamma c \left(2\pi\alpha_{\mathrm{B}}\frac{A}{R^s}\right)^{1/2} \simeq 8\left(\frac{\alpha_{\mathrm{B}}}{0.01}\right)^{1/2}\left(\frac{\Gamma}{100}\right)\left(\frac{n}{1\ \mathrm{cm}^{-3}}\right)^{1/2}\ \mathrm{G}\ . \tag{4.14}$$

We also assume that a fraction α_{e} of the internal energy is injected in the electrons :

$$n_{\mathrm{e}}\bar{\Gamma}_{\mathrm{e}} m_{\mathrm{e}} c^2 \simeq \alpha_{\mathrm{e}}\ \frac{4\Gamma A}{R^s}\ \Gamma c^2\ , \tag{4.15}$$

where the total electron density $n_{\rm e}$ is given by $n_{\rm e}=\rho_*/m_{\rm p}\simeq 4\Gamma A/(m_{\rm p}R^s)$. Therefore the electrons get a mean Lorentz factor :

$$\bar{\Gamma}_{\rm e}\simeq\alpha_{\rm e}\frac{m_{\rm p}}{m_{\rm e}}\Gamma\simeq 1.8\ 10^4\ \left(\frac{\alpha_{\rm e}}{0.1}\right)\left(\frac{\Gamma}{100}\right)\ . \tag{4.16}$$

We assume that the electron distribution just behind the shock follows a power-law starting at Lorentz factor $\Gamma_{\rm i}$:

$$n(\Gamma_{\rm e}) \propto \Gamma_{\rm e}^{-p}\ \text{for}\ \Gamma_{\rm e}\geq\Gamma_{\rm i}\ , \tag{4.17}$$

$$\text{with}\ \Gamma_{\rm i} = \frac{p-2}{p-1}\bar{\Gamma}_{\rm e}\ . \tag{4.18}$$

Of course these estimates should be confirmed by a more detailed description of the physical conditions in the shocked medium, including the microphysics leading to the magnetic field amplification and the electrons acceleration.

Synchrotron radiation : the electrons moving in the magnetic field radiate by the synchrotron process. The synchrotron power of an electron with Lorentz factor $\Gamma_{\rm e}$ is given by [43]:

$$P_{\rm syn}\left(\Gamma_{\rm e}\right)=\frac{4}{3}\sigma_{\rm T}c\ \frac{B^2}{8\pi}\ \Gamma_{\rm e}^2 \tag{4.19}$$

and the typical energy of the emitted photons is (in the observer frame)

$$h\nu_{\rm syn}\left(\Gamma_{\rm e}\right) = \Gamma\ \frac{3he}{2\pi m_{\rm e}c}B\Gamma_{\rm e}^2 \tag{4.20}$$

$$\simeq 9.0\left(\frac{\alpha_{\rm B}}{0.01}\right)^{1/2}\left(\frac{\alpha_{\rm e}}{0.1}\right)^2\left(\frac{\Gamma}{100}\right)^4\left(\frac{n}{1\ {\rm cm}^{-3}}\right)^{1/2}{\rm keV}\ . \tag{4.21}$$

Then the radiative timescale, defined as the time necessary for an electron to lose all its energy by radiation, is (in the comoving frame):

$$t'_{\rm syn}\left(\Gamma_{\rm e}\right)=\frac{\Gamma_{\rm e}m_{\rm e}c^2}{P_{\rm syn}\left(\Gamma_{\rm e}\right)}\simeq 770\ \left(\frac{B}{10\ {\rm G}}\right)^{-2}\left(\frac{\Gamma_{\rm e}}{10^4}\right)^{-1}\ {\rm s}\ . \tag{4.22}$$

This timescale has to be compared with the adiabatic cooling time, defined as the time necessary for the shocked medium to cool adiabatically due to spherical expansion :

$$t'_{\rm ex}\simeq\frac{R}{\Gamma c}\simeq 3.3\ 10^4\ \left(\frac{R}{10^{17}\ {\rm cm}}\right)\left(\frac{\Gamma}{100}\right)^{-1}\ {\rm s}\ . \tag{4.23}$$

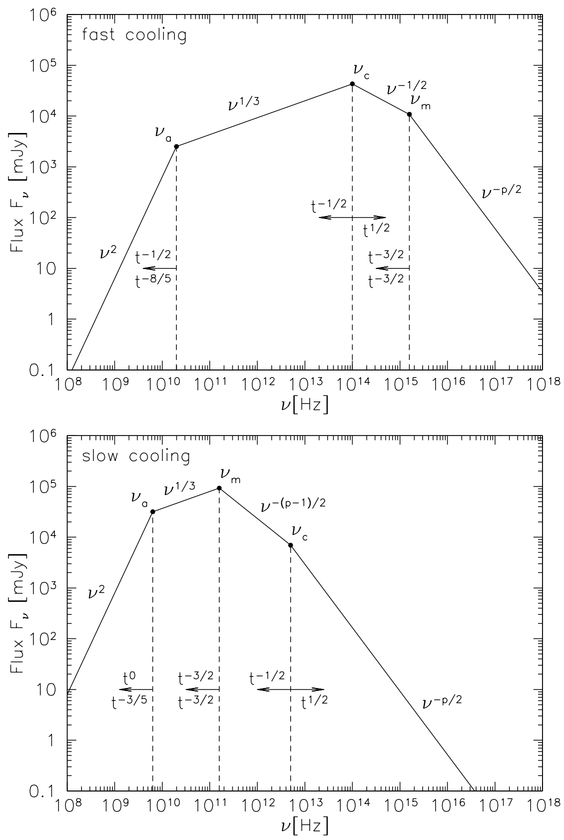

Fig. 24. The synchrotron spectrum. *Upper panel :* "fast cooling" regime ; *Lower panel :* "slow cooling" regime. The spectral breaks $\nu_{\rm m}$ and $\nu_{\rm c}$ corresponds respectively to the synchrotron frequency of electrons with Lorentz factor $\Gamma_{\rm i}$ and $\Gamma_{\rm c}$ (see text). The frequency $\nu_{\rm a}$ corresponds to the break due to synchrotron self-absorption. The time dependance of these frequencies is given for a uniform medium $s = 0$ (above the arrows) and for a stellar wind $s = 2$ if different (bellow the arrows) (from [44]).

As pointed by Sari et al. [44], there are two possible regimes : (i) initially, the radiative timescale is very short and all electrons radiate efficiently ("fast cooling" regime) ; (ii) once the magnetic field and the electron energy have decreased, the radiative timescale of most of the electrons becomes larger than the adiabatic cooling time and only the highest energy electrons (which have the shortest radiative timescale) can still radiate efficiently ("slow cooling" regime). A given electron will radiate efficiently as long as

$t'_{\rm syn} \ll t'_{\rm ex}$, which gives the condition :

$$\Gamma_{\rm e} \gg \Gamma_{\rm c} = \frac{6\pi m_{\rm e} c}{\sigma_{\rm T} B^2 t'_{\rm ex}}\ . \tag{4.24}$$

The "fast cooling" regime corresponds to $\Gamma_{\rm i} \gg \Gamma_{\rm c}$ – all electrons can radiate their total energy in less than the adiabatic cooling time – and the "slow cooling " regime corresponds to $\Gamma_{\rm i} \ll \Gamma_{\rm c}$ – only high-energy electrons with $\Gamma_{\rm e} > \Gamma_{\rm c}$ can radiate effiently ; most of the energy, which is contained in low-energy electrons, is not radiated. These two regimes lead to two different spectral shapes, described in figure 24. The resulting observed flux at frequency ν follows

$$f_\nu \propto \nu^\alpha t^\beta\ , \tag{4.25}$$

which is in good agreement with the observations (see section 2). The slopes α and β are given in figure 24.

4.3 Additional effects

Geometric beaming : the basic description which has been made in the last two subsections needs a few improvements to become more realistic. The most important effect is due to the probable non-spherical symmetry of the relativistic ejecta, as first pointed out by Rhoads [45]. Figure 25 illustrates this effect : due to relativistic beaming, the observer can only detect photons coming from a small fraction of the emitting surface, this region being centered on the line of sight and having an opening angle $\sim 1/\Gamma$. Initially, except for a highly beamed ejecta, this opening angle is small compared to the geometrical opening angle of the ejecta θ_0. Therefore, the observer cannot see any difference in this period between a spherical and a beamed emitting surface (the prompt GRB is entirely produced during this period). However, the deceleration due to the external medium makes the Lorentz factor Γ decrease and then the angle $1/\Gamma$ increase. The observer can see the whole emitting surface for the first time in the history of the GRB at the time when $1/\Gamma \simeq \theta_0$. This should appear as a break in the lightcurve since a fraction of the photons emitted on the edge of the surface are now not suffiently beamed to be detected. An additional physical effect has to be taken into account and makes this picture a little more complex: the lateral expansion of the ejecta. The geometrical opening angle of the relativistic ejecta is not kept constant to θ_0 during the whole evolution. However, it can be shown that this lateral expansion becomes important more or less at the same period when when $1/\Gamma \sim \theta_0$.

The observations indeed show breaks in the lightcurve that can be interpreted as resulting from this effect (one important signature which confirms that a given break is due to this geometrical effect is that it is expected

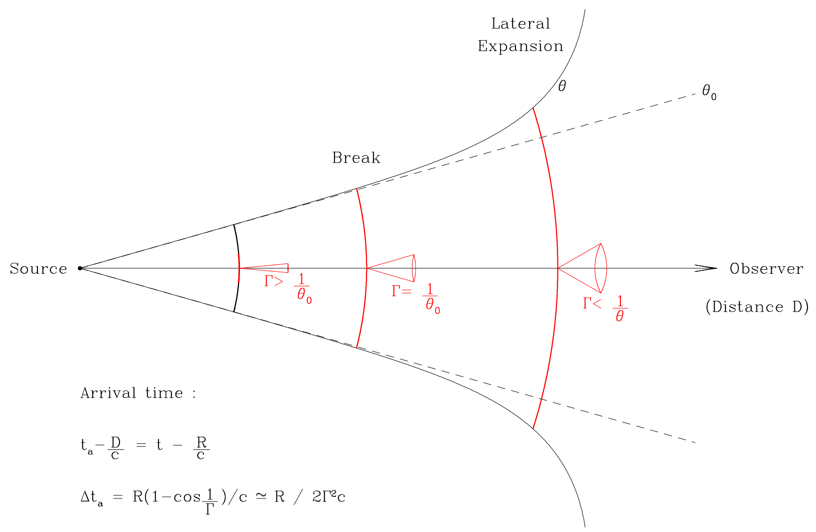

Fig. 25. Geometrical beaming vs relativistic beaming.

to be achromatic, i.e. observed at the same time at all frequencies). If the break time is precisely identified, one can then try to estimate the corresponding Lorentz factor and the initial beaming angle of the relativistic ejecta $\theta_0 \simeq 1/\Gamma$, which in the case of a uniform medium ($s = 0$) is given by

$$\theta_0 \simeq 2^\circ \left(\frac{t_a(\text{break})}{0.8\,(1+z)\ \text{days}}\right)^{3/8} \left(\frac{E}{10^{53}\ \text{erg}}\right)^{-1/8} \left(\frac{n}{1\ \text{cm}^{-3}}\right)^{-1/8} . \quad (4.26)$$

This allows to estimate the beaming fraction f_Ω defined in section 2 and then the true energy radiated during the burst. This has been done for a few GRBs listed in table 3 [33]. The result seems to indicate that the large dispersion of the isotropic equivalent energy radiated in gamma-rays comes mainly from a large dispersion in the opening angle, the true energy radiated in gamma-rays being remarkably concentrated around $5\ 10^{50}$–10^{51} erg. This study suffers of course many limitations, the main one being that the break is clearly identified in several spectral bands in only four cases (marked in bold face in table 3). In all other cases, either the break is detected in only one band, which is not unambiguous, or even worse, only a limit on the break time could be derived, by explaining the observed slope of the lightcurve as a pre- or post-break slope.

GRB	Redshift	$E_{\gamma,4\pi}$ (10^{51} erg)	$t_{\rm a}$(break) (days)	θ_0 ($^\circ$)	E_γ (10^{51} erg)
970228	0.695	22.4	...	...	...
970508	0.835	5.46	25.	16.8	0.234
970828	0.958	220.	2.2	4.13	0.575
971214	3.418	211.	> 2.5	> 3.21	> 0.333
980613	1.096	5.67	> 3.1	> 7.28	> 0.045
980703	**0.966**	**60.1**	**7.5**	**7.73**	**0.544**
990123	1.600	1440	2.04	2.86	1.80
990506	1.30	854	...	...	...
990510	**1.619**	**176.**	**1.20**	**3.04**	**0.248**
990705	0.84	270.	~ 1	3.09	0.389
990712	0.433	5.27	> 47.7	> 23.5	> 0.445
991208	0.706	147	< 2.1	< 4.53	< 0.455
991216	1.02	535	1.2	2.92	0.695
000131	4.500	1160	< 3.5	< 2.69	< 1.30
000301C	**2.034**	**46.4**	**5.5**	**6.02**	**0.256**
000418	**1.119**	**82.0**	**25.**	**11.3**	**1.60**
000926	2.037	297	1.45	2.92	0.379

Table 3. Sample of 17 afterglows studied by Frail et al. [33] : redshift, isotropic equivalent energy radiated in gamma-rays, break time, opening angle and true energy radiated in gamma-rays.

Other effects : A realistic afterglow model has to take into account many other processes : effect of radiative losses on the shock dynamics, changes in the photon spectrum due to inverse compton scatterings, modification of the high-energy spectrum due to the maximum Lorentz factor of the electrons, etc... An exemple of a detailed calculation taking into account all these effects can be found in Panaitescu & Kumar [46]. The result obtained in the case of GRB 980703 is plotted in figure 26. Such multiwavelength fits could in principle be used to estimate all important parameters, such as the density of the external medium, the initial energy and Lorentz factor of the relativistic ejecta, etc.. However, it seems that the available data can only poorly constrain most of these parameters. In particular, it is often difficult to distinguish between a $s = 0$ or a $s = 2$ external medium. This is mainly due to the lack of early multiwavelength observations and should be improved in the coming years.

Long-term evolution : Hydrodynamical 2D-simulations of the long-term evolution of the GRB remnant in the non-relativistic phase have been carried by Ayal & Piran [47]. Their main result is that an initially beamed

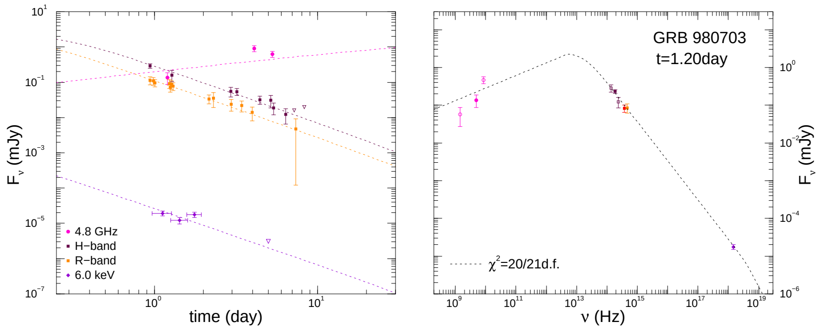

Fig. 26. GRB 980713 : result of a detailed multiwavelength fit of the afterglow [46]. The best-fit parameters are $E = 2.9\ 10^{54}$ erg, $\theta_0 \geq 2.7^\circ$, $s = 0$, $n = 7.8\ 10^{-4}\ \mathrm{cm}^{-3}$, $\alpha_{\mathrm{B}} = 4.6\ 10^{-4}$, $\alpha_{\mathrm{e}} = 0.075$ and $p = 3.08$. The authors mention that a good fit with $s = 2$ is also possible.

relativistic ejecta becomes spherical at a time

$$t_{\mathrm{a}} \simeq 3000 \left(\frac{E}{10^{51}\ \mathrm{erg}}\right)^{1/3} \left(\frac{n}{1\ \mathrm{cm}^{-3}}\right)^{-1/3}\ \mathrm{yr}\ . \tag{4.27}$$

The radius of the sphere is then

$$R \simeq 12 \left(\frac{E}{10^{51}\ \mathrm{erg}}\right)^{1/3} \left(\frac{n}{1\ \mathrm{cm}^{-3}}\right)^{-1/3}\ \mathrm{pc}\ . \tag{4.28}$$

At this stage, it is very difficult to distinguish the GRB remnant from a supernova remnant.

5 Prompt emission

If most of the current models of GRBs agree about the physical origin of the afterglow – deceleration of an ultra-relativistic ejecta by its environment as described in section 4 – the situation is not so clear concerning the origin of the GRB itself. However, we will not describe all proposed models for the prompt emission in this lecture but rather concentrate on a particular one, the internal shock model, which is probably the model which has been studied most extensively and which seems to correctly reproduce most of the observed properties of GRBs. We will then discuss the possible contribution of the reverse shock, which is formed together with the external shock as mentioned in section 4, to the prompt emission and we will end this section by an estimate of the thermal precursor emitted when the relativistic ejecta becomes transparent at the end of the acceleration phase.

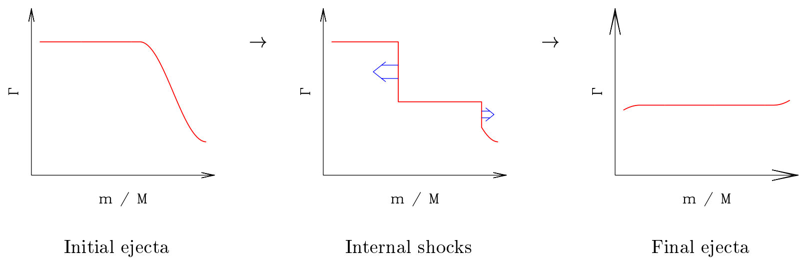

Fig. 27. The internal shock model : *Left :* in this simple example, the relativistic ejecta is initially produced with a "slow" part ahead of a "rapid" part. *Center :* the rapid part catches up with the slow one and two shocks appear : a forward and a reverse shock. These two "internal shocks" propagate within the ejecta and the shocked matter radiate to produce the GRB. *Right :* Once the two waves have crossed the ejecta, the Lorentz factor is ordored with rapid layers at the front : the internal shock phase stops. The burst produced in this example is made of a single pulse burst. The complex observed profiles are due to relativistic ejecta with much more variable Lorentz factors.

5.1 Internal shocks

5.1.1 A simple model

The internal shock model has been proposed in 1994 by Rees and Meszáros [48]. The main assumption is that the relativistic ejecta emitted by the central source is produced with a highly variable distribution of the Lorentz factor, varying on timescales possibly as short as the dynamical timescale of the central engine. As the central object is most probably a stellar-mass black hole of mass M_{BH} surrounded by an accretion disk (see section 6), this timescale is of the order of

$$t_{\mathrm{var}} \simeq \frac{6GM_{\mathrm{BH}}}{c^3} \simeq 0.3 \left(\frac{M_{\mathrm{BH}}}{10\ \mathrm{M}_{\odot}}\right)\ \mathrm{ms}\ . \tag{5.1}$$

The fastest shells in the relativistic ejecta (highest Γ) catch up with the slowest ones (lowest Γ) which leads to the formation of shock waves propagating within the relativistic ejecta, the so-called "internal shocks". The hot matter behind the shocks radiate and produce the prompt GRB emission. This phase naturally stops when the ejecta is ordered, the Lorentz factor decreasing from the front to the back of the ejecta. This is illustrated in figure 27.

Description of the relativistic outflow. In a first simple version of the model [49], we consider that the relativistic ejecta is made of shells emitted regularly by the central source on a timescale $t_{\rm var}$. Each shell has a Lorentz factor $\Gamma_{\rm i}$, a mass $M_{\rm i}$ and an energy $E_{\rm i}=\Gamma_{\rm i}M_{\rm i}c^2$. Here all quantities have their isotropic equivalent values. We also assume that the central engine is active for a total duration $t_{\rm w}$ so that the number of shells is $N=t_{\rm w}/t_{\rm var}$ and that the total width of the relativistic ejecta is initially $\Delta\sim ct_{\rm w}$. The total mass and energy are $M=\sum_{\rm i}M_{\rm i}$ and $E=\sum_{\rm i}E_{\rm i}$ and the averaged value of the Lorentz factor $\bar{\Gamma}=E/Mc^2$. The Lorentz factor $\Gamma_{\rm i}$ is highly variable with the condition that $\bar{\Gamma}\gtrsim 100$, which was derived from the spectral observations in section 2. These relativistic shells are "solid" : they only interact by direct collisions so that all pressure waves are neglected. This very crude assumption has been validated by more realistic hydrodynamical simulations [50]. The succession of these direct collisions between shells represent the propagation of shock waves within the relativistic ejecta, i.e. internal shocks.

Typical radius and observed timescales. If a shell 2 (Lorentz factor Γ_2) is emitted a time $t_{\rm var}$ after a shell 1 (Lorentz factor $\Gamma_1<\Gamma_2$), a collision occurs a the radius

$$R_{12}\simeq 2\frac{\Gamma_1^2\Gamma_2^2}{\Gamma_2^2-\Gamma_1^2}\ ct_{\rm var}\ . \tag{5.2}$$

This allows to derive the typical radius of the internal shocks :

$$R_{\rm IS}\simeq 2f^2\bar{\Gamma}^2ct_{\rm var}\simeq 6\ 10^{14}\ f^2\left(\frac{\bar{\Gamma}}{100}\right)^2\left(\frac{t_{\rm var}}{1\ \rm s}\right)\ \rm cm\ , \tag{5.3}$$

where f is a coefficient depending on the shape of the initial Lorentz factor distribution. This coefficient is smaller than unity and of the order of $\Gamma_{\rm min}/\bar{\Gamma}$, where $\Gamma_{\rm min}$ is the minimum value of the initial Lorentz factor. Photons emitted along the line of sight by an internal shock at radius R and time t will be observed at the "arrival time" $t_{\rm a}=t-R/c$ already defined in the previous sections (see figure 25). Photons emitted at the same R and t on the edge of the "visible" fraction of the emitting surface will be detected at time $t_{\rm a}+\Delta t_{\rm a}$ with $\Delta t_{\rm a}\simeq R/2c\Gamma^2$, where Γ is the Lorentz factor of the emitting material. This means that even an impulsive emission is observed with a non zero duration $\Delta t_{\rm a}$ which is then the shortest timescale that one can observe in the GRB profiles. From the estimate of the typical internal shock radius, it is easy to see that $t_{\rm a}$ as well as $\Delta t_{\rm a}$ are of the order of

$$t_{\rm a}\sim\Delta t_{\rm a}\sim f^2t_{\rm var}\ . \tag{5.4}$$

The $\bar{\Gamma}^2$ factor has disappeared, which is not surprising as this property was already used in section 3 to solve the compactness problem. Equation 5.4 has two fundamental consequences [49,51] : (i) **the ability of the internal shock model to reproduce the observed variability.** If the shortest timescale of variation in the initial distribution of the Lorentz factor is of the order of the dynamical timescale of the central source as estimated above, then variability in the GRB time profiles can be observed down to this time scale (corrected with the f coefficient and the redshift time dilation). (ii) **the origin of the observed duration of the GRB :** if the shortest variations in the GRB time profiles are related to the shortest timescales of variation in the initial distribution of the Lorentz factor, conversely the total burst duration is related to the largest timescale, i.e. to the total duration of the central source activity t_{w}. It means that in the internal shock model, a short burst of 0.1 s has been produced by a source active for about $0.1/(1+z)$ s and a long burst of 10 s by a source active for about $10/(1+z)$ s. This is of course a constraint for the models of central engine: (a) the bimodal distribution of the observed duration should correspond to two class of sources with different characteristic timescales ; (b) if they are also produced by internal shocks, the longest bursts (more than 100 s) correspond to central engines active for very long durations (compared to their dynamical timescale), which is a severe constraint. Notice that equation 5.3 indicates that for t_{var} varying from ~ 1 ms to ~ 10 s, the internal shock phase occurs on a large interval of radii, from $\sim 10^{11}$ to $\sim 10^{16}$ cm, depending on the average value of the Lorentz factor.

Description of a two shell collision. The physics of the internal shocks is close to the physics of the external shock described in section 4, with an important difference : these shocks are only midly relativistic as there are produced by the interaction between shells with relative velocities of about 0.5-0.8c. In particular, the shock conditions written in equations 4.6, 4.7 and 4.8 are not valid any more. We will see below that the specific internal energy in the shocked material can be estimated to be much less that in the case of the external shock (see equation 4.7 and 5.7 below).
In the simple description considered here, when a collision between two shells of mass and Lorentz factor Γ_1, M_1 and Γ_2, M_2 occur, the two shells merge to produce a new shell of mass $M_1 + M_2$ and Lorentz factor Γ_{r}. This Lorentz factor can be computed from the conservation of the energy-momentum quadri-vector (inelastic collision) and is given by

$$\Gamma_{\mathrm{r}} = \sqrt{\Gamma_1\Gamma_2}\sqrt{\frac{M_1\Gamma_1 + M_2\Gamma_2}{M_1\Gamma_2 + M_2\Gamma_1}}\ , \tag{5.5}$$

which becomes $\Gamma_{\mathrm{r}} = \sqrt{\Gamma_1\Gamma_2}$ when $M_1 = M_2$. The dissipated energy during the collision can then be obtained :

$$e = \left(\Gamma_1 M_1 c^2 + \Gamma_2 M_2 c^2\right) - \Gamma_{\mathrm{r}}\left(M_1 + M_2\right) c^2\ . \tag{5.6}$$

The corresponding efficiency $e/\left(\Gamma_1 M_1 c^2 + \Gamma_2 M_2 c^2\right)$ is typically a few 10 %, depending on the contrast between the two Lorentz factors. This dissipated energy is initially present in the shocked material as internal energy. One can estimate the corresponding specific internal energy in the comoving frame, which for $M_1 = M_2$ is :

$$\epsilon_* \simeq \left[\frac{1}{2}\left(\sqrt{\frac{\Gamma_1}{\Gamma_2}}+\sqrt{\frac{\Gamma_2}{\Gamma_1}}\right)-1\right]c^2 \simeq 240 \text{ MeV/proton for } \Gamma_2/\Gamma_1 = 4 \ . \tag{5.7}$$

This is much less than in the early afterglow as expected because of the midly relativistic nature of the internal shocks. As in section 4, we assume that a fraction α_e is injected into relativistic electrons, with the difference that only a fraction ζ of the electrons is accelerated in a non-thermal power-law distribution. There are some theoretical arguments derived from the physics of non relativistic MHD shocks to expect such a behaviour [52]. This leads to an averaged value of the electron Lorentz factor equal to

$$\bar{\Gamma}_\mathrm{e} \simeq \frac{\alpha_\mathrm{e}}{\zeta}\frac{m_\mathrm{p}}{m_\mathrm{e}}\frac{\epsilon_*}{c^2} \simeq 40\ \left(\frac{\alpha_\mathrm{e}/\zeta}{0.1}\right)\left(\frac{m_\mathrm{p}\epsilon_*}{200\text{ MeV}}\right)\ . \tag{5.8}$$

This indicates that the acceleration is not very efficient if the fraction ζ is high ($\bar{\Gamma}_\mathrm{e}$ in the range 10-100). On the other hand, for small values of ζ, the accelerated electrons can of course be much more energetic (equation 5.8 gives $\bar{\Gamma}_\mathrm{e} \sim 4\ 10^4$ for $\alpha_\mathrm{e}/\zeta = 100$). The magnetic field strength can also be estimated by assuming that the magnetic energy corresponds to a fraction α_B of the internal energy :

$$B \simeq \sqrt{8\pi\alpha_\mathrm{B}\rho_*\epsilon_*}\ . \tag{5.9}$$

The density ρ_* of the shocked material can be obtained in this simple version of the model by

$$\rho_* \simeq \frac{E}{\bar{\Gamma}^2 4\pi R_\mathrm{IS}^2 c^3 t_\mathrm{w}}\ , \tag{5.10}$$

leading to typical magnetic field of about $100\sqrt{\alpha_\mathrm{B}}$ to $10^4\sqrt{\alpha_\mathrm{B}}$ G. It is important to notice that the magnetic field in several scenarios can be very different from this estimate if a large scale magnetic field anchored in the central source is also present [53].

Radiative processes. As the observed spectra are non-thermal, this is a difficult task to understand the details of the radiative processes operating during the internal shock phase. This question is still under debate and we will only make here a few estimates and then point out in the results what are the main problems that a more realistic description of these processes should solve.

– *The "inverse Compton" case :* As the synchrotron process seems to be dominant in the afterglow phase, it is natural to imagine that it plays also a role in the internal shock phase. If all electrons are accelerated ($\zeta \sim 1$), equation 5.8 gives $\bar{\Gamma}_{\mathrm{e}} \sim 100$ and from equation 4.20, the typical energy of synchrotron photons is given by (in the observer frame) :

$$E_{\mathrm{syn}} \simeq 17 \left(\frac{\Gamma_{\mathrm{r}}}{100}\right) \left(\frac{B}{1000\ \mathrm{G}}\right) \left(\frac{\bar{\Gamma}_{\mathrm{e}}}{100}\right)^2 \ \mathrm{eV}\ , \tag{5.11}$$

which typically corresponds to UV photons, well below the spectral range of the observed GRBs. The gamma-ray photons can then be produced by inverse Compton scattering of the UV synchrotron photons by the relativistic electron. At these energies we are in the Thomson limit and the resulting typical energy of the scattered photons is

$$E_{\mathrm{ic}} \simeq 170 \left(\frac{\Gamma_{\mathrm{r}}}{100}\right) \left(\frac{B}{1000\ \mathrm{G}}\right) \left(\frac{\bar{\Gamma}_{\mathrm{e}}}{100}\right)^4 \ \mathrm{keV}\ , \tag{5.12}$$

which is now in the expected spectral range corresponding to the observed peak energy of GRBs. It is of course important to check that the inverse Compton photons carry most of the emitted energy. This is done by computing the optical depth of the emitting material for this process. The result is that the fraction f_{ic} of the emitted energy which is radiated by the inverse Compton process is given by the following equation (for a detailed derivation, see [49]) :

$$f_{\mathrm{ic}}^2 - \left(2 + \frac{3}{8}\frac{\alpha_{\mathrm{B}}}{\alpha_{\mathrm{e}}}\right) f_{\mathrm{ic}} + 1 \simeq 0\ . \tag{5.13}$$

Equipartition ($\alpha_{\mathrm{e}} \sim \alpha_{\mathrm{B}}$) then gives a moderate efficiency $f_{\mathrm{ic}} \sim 0.55$. A weak magnetic field is required to increase f_{ic} : $\alpha_{\mathrm{B}}/\alpha_{\mathrm{e}} \sim 10^{-3}$ leads to $f_{\mathrm{ic}} \sim 0.98$.

– *The "synchrotron" case :* If we now assume that the fraction ζ is low, the typical Lorentz factor of the electron can be much higher than in the previous case and equation 4.20 gives

$$E_{\mathrm{syn}} \simeq 170 \left(\frac{\Gamma_{\mathrm{r}}}{100}\right) \left(\frac{B}{1000\ \mathrm{G}}\right) \left(\frac{\bar{\Gamma}_{\mathrm{e}}}{10^4}\right)^2 \ \mathrm{keV}\ . \tag{5.14}$$

In this case, the observed prompt gamma-ray emission can be directly produced by the synchrotron process. The inverse Compton scattered photons are now produced in the Klein-Nishina regime and have a typical energy

$$E_{\mathrm{ic}} \simeq 500 \left(\frac{\Gamma_{\mathrm{r}}}{100}\right) \left(\frac{\bar{\Gamma}_{\mathrm{e}}}{10^4}\right) \ \mathrm{GeV}. \tag{5.15}$$

We have of course to check that the fraction $f_{\rm syn}$ of the energy which is radiated by the synchrotron process is high. Due to the Klein-Nishina regime, the equation defining $f_{\rm syn}$ is not so simple than equation 5.13 :

$$\frac{1+\ln\left(2w\right)}{w^2}\frac{\alpha_{\rm e}}{\alpha_{\rm B}}\ f_{\rm syn}^2+f_{\rm syn}-1=0\ , \tag{5.16}$$

where $w\simeq\bar{\Gamma}_{\rm e}E_{\rm syn}/\left(\Gamma_{\rm r}m_{\rm e}c^2\right)\gg 1$. Calculations show that during most of the burst $f_{\rm syn}$ is very close to unity due to the decrease of the scattering cross section in the Klein-Nishina regime [49].

Radiative efficiency : the fraction $f_{\rm rad}$ of the energy $\alpha_{\rm e}\times e$ injected in the non-thermal electrons that is radiated can be easily obtained from the comparision between the adiabatic cooling time $t'_{\rm ex}$ defined in section 4 and the radiative timescale, which is $f_{\rm syn}t'_{\rm syn}$ in the two cases presented just above. Simulations show that electrons are in the "fast cooling" regime during most of the burst so that $f_{\rm rad}$ is very close to unity [49].

Synthetic gamma-ray bursts : for each two shell collision, the dissipated energy e and the arrival timeof photons $t_{\rm a}$ can be computed. If we then assume an elementary spectral shape (i.e. for the synchrotron case a broken power-law spectrum, corresponding to the "fast cooling" case in figure 24), the elementary contribution of each single collisions to the burst is now entirely fixed. A synthetic GRB can be produced by summing all these elementary contributions. This allows to compute its lightcurve and spectrum and to compare them to the observations. The total dynamical efficiency of the internal shock phase can be also computed :

$$f_{\rm d}\simeq\frac{\sum_{\rm collisions}e}{E}\ , \tag{5.17}$$

and is typically of a few 10 %. To get the total efficiency $f_{\rm tot}$ of the internal shocks, $f_{\rm d}$ has to be multiplied by $f_{\rm rad}\times\alpha_{\rm e}\times f_{\rm BATSE}$, where $f_{\rm BATSE}$ is the fraction of the radiated energy which is emitted in the BATSE spectral range. The result is a low efficiency, with $f_{\rm tot}$ of a few percents only...

5.1.2 Hydrodynamical model :

The simple model presented above offers the advantage to allow the simulation of many synthetic bursts in a very short computing time. However the very simplifying assumptions which have been made have to be validated. Hydrodynamical relativistic simulations – where the complete evolution of an ejecta with a highly variable Lorentz factor is followed from the saturation radius $R_{\rm sat}$ (where the acceleration is complete) to the deceleration radius $R_{\rm dec}$ (where the deceleration by the external medium starts) – allow

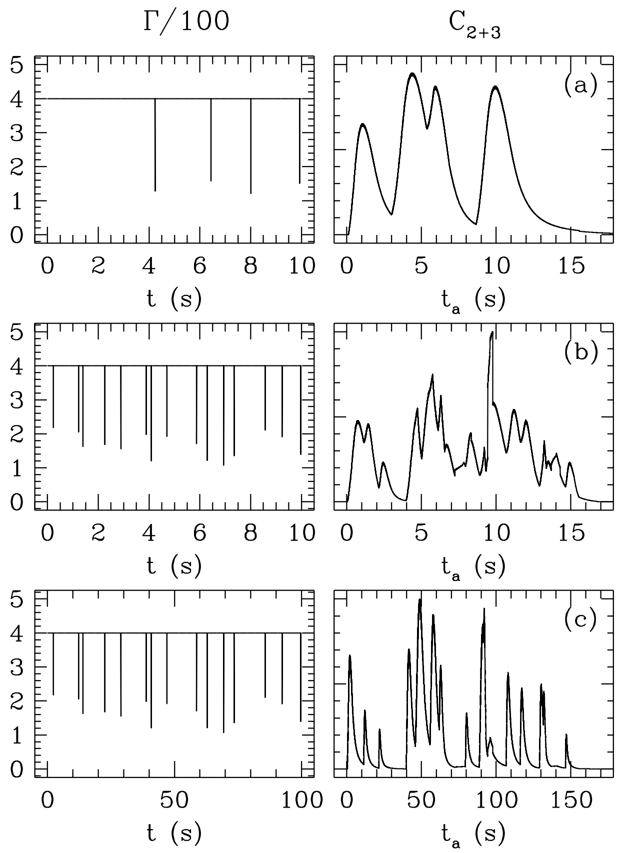

Fig. 28. Three synthetic GRB time profiles. *Left column :* the initial distribution of the Lorentz factor in the relativistic ejecta. *Right column :* the corresponding time profile in the 2+3 band of BATSE. The adopted redshift is $z = 0.5$. In the three cases, the relativistic outflow has a more or less constant Lorentz factor $\Gamma = 400$, with a few slower layers with Lorentz factors between 100 and 400. The number of slow layers is higher in the last two cases and the corresponding profile more complex. Notice that case (c) is similar to case (b) with all timescales shifted by a factor of ten. (from [49])

to follow properly the internal shock phase and to compute in a consistent way the density and the internal energy density in the shocked material. The results are in a very good agreement with the results of the simple model [50], probably because the dynamics is completely dominated by the kinetic energy of the flow so that pressure waves do not play a major role.

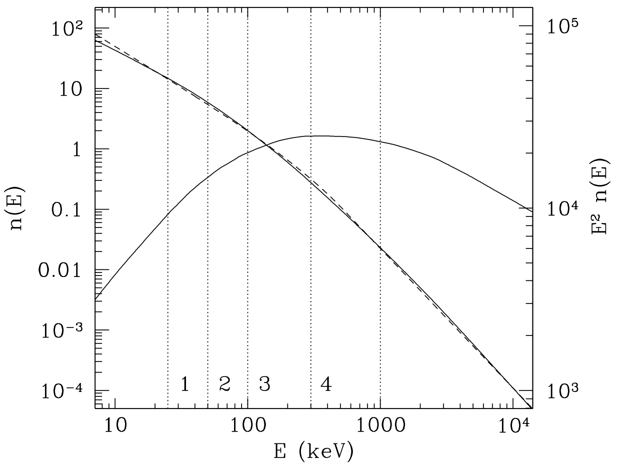

Fig. 29. Synthetic spectrum corresponding to case (a) in figure 29. (From [49])

5.1.3 Results :

The simulation of synthetic GRBs and the comparison of their properties with the observations lead to the following results : (i) the temporal properties of GRBs are very well reproduced, including the variability of the time profiles and the asymmetry of the elementary pulses. In this model, the light curve can be seen as reflecting the variable activity of the central engine ; (ii) the spectral properties are satisfactory, the peak energy and the global shape of the spectrum being in agreement with the observations, but a major problem remains : the predicted low energy slope is very close to $\alpha \sim -1.5$ and the distribution of α shown in figure 7 is not reproduced. It is hoped that this problem can be solved with a more detailed description of the radiative processes ; (iii) most observed relations between the temporal and the spectral properties are reproduced, including the hardness ratio – duration correlation, the evolution of the pulse shape with the energy band, the photon fluence – peak energy correlation, etc [49,50]. Another difficulty of the model is the low total efficiency of the mechanism, which implies very powerful and efficient central engines. Three examples of synthetic GRB lightcurves are presented in figure 28. The global spectrum corresponding to case (a) in figure 28 is shown in figure 29. The peak energy is 365 keV and the dotted line shows the best-fit by the Band spectral model. Figure 30 shows an example of a single pulse burst which illustrates how the pulses properties are reproduced by the model. Figure 31 shows the hardness ratio H_{32} – duration T_{90} relation, obtained with sequences of models where only the duration $t_{\rm w}$ is varied.

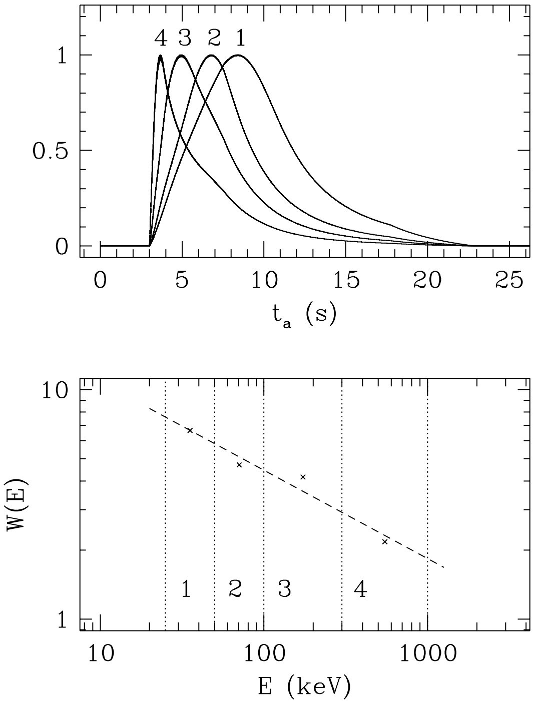

Fig. 30. A synthetic single pulse burst in the four BATSE energy bands. The pulse is peaking earlier at high energy (band 4) and its width $W(E)$ is decreasing with the energy band (lower panel), in agreement with the observations. (From [49])

Despite these encouraging results, many aspects of the model have still to be better understood, mainly the radiative processes. A difficulty is that because of the lack of prompt observations at other wavelength, it is very difficult to distinguish between the "inverse Compton" and the "synchrotron" cases presented above. The synchrotron case may be prefered due to a somewhat better total efficiency. Of course, the detection of a high-energy second peak in the spectrum, for instance by GLAST, would very rapidly solve this question. Another approach is to study the details of the pulses properties, especially the HIC and the HFC presented in section 2, to put some constraints on the physical processes at work in the shocked medium. Recently, this approach has allowed to propose a small modification of the standard $\alpha_{\rm e}$, $\alpha_{\rm B}$, ζ prescription that leads to an excellent agreement between the synthetic pulse evolution and the observations [54].

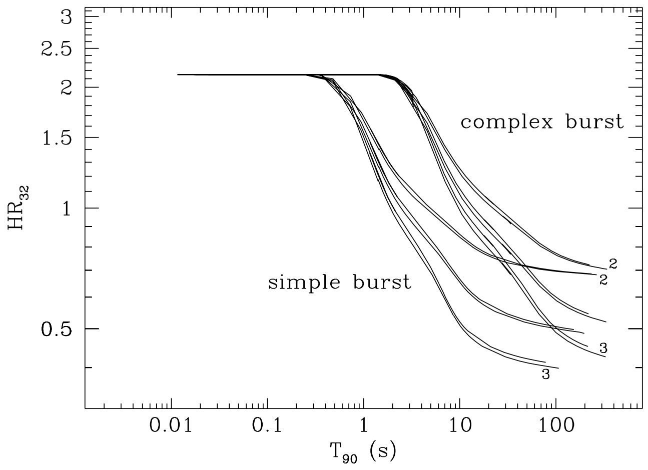

Fig. 31. Hardness ratio H_{32} as a function of the burst duration T_{90}. Each line corresponds to a sequence of models where only the duration t_{w} of activity of the central source is varied. Two different initial distribution of the Lorentz factor have been considered : a simple one leading to a single pulse burst ("simple burst") and a more complex one leading to a five pulses burst ("complex burst"). In each case, the sequence has been computed for three high-energy index β (-2, -2.5 and -3) and two different redshifts (the two corresponding curves are very close). (From [49])

5.2 Reverse shock

5.2.1 Physics of the reverse shock

Dynamics. As described in section 4, the reverse shock appears together with the external shock, at the deceleration radius R_{dec}. However, as it propagates within the relativistic ejecta, its physics is very close to that of internal shocks (in particular the reverse shock is usually only midly relativistic). The Lorentz factor of the reverse shock is given by [55] :

$$\Gamma_{\mathrm{RS}} \simeq \left(\frac{\bar{\Gamma}}{2}\right)^{1/2} \left(\frac{\bar{\rho}}{\rho_{\mathrm{ext}}}\right)^{1/4} , \tag{5.18}$$

where $\bar{\rho}$ is the averaged density in the relativistic ejecta. Therefore, the reverse shock has entirely crossed the relativistic ejecta (whose width is $\Delta \sim ct_{\mathrm{w}}$) at radius

$$R_{\mathrm{cross}} \simeq \Gamma_{\mathrm{RS}}^2 \Delta \simeq \sqrt{R_{\mathrm{dec}} R_{\mathrm{IS}}} , \tag{5.19}$$

where $R_{\rm dec}$ is given by equations 4.4 ($s=0$) and 4.5 ($s=2$) and $R_{\rm IS}$ is the radius of the last internal shocks:

$$R_{\rm IS} \simeq 2f^2\bar{\Gamma}^2 c t_{\rm w} \simeq 6\ 10^{15}\ f^2\ \left(\frac{\bar{\Gamma}}{100}\right)^2 \left(\frac{t_{\rm w}}{10\ \rm s}\right)\ \rm cm\ . \tag{5.20}$$

From the expression of $R_{\rm cross}$, it is clear that there is a unique condition to have distinct reverse shock and internal shock phases : $R_{\rm dec} > R_{\rm IS}$. This condition can be written as [56]

$$Q = \left(\frac{R_{\rm dec}}{R_{\rm IS}}\right)^{3-s} > 1\ , \tag{5.21}$$

which leads to the following condition for a uniform medium ($s=0$) :

$$Q \simeq 7.2\ 10^3\ f^{-6}\ \left(\frac{E}{10^{53}\ \rm erg}\right)\left(\frac{n}{1\ \rm cm^{-3}}\right)\left(\frac{\bar{\Gamma}}{100}\right)^{-8}\left(\frac{t_{\rm w}}{10\ \rm s}\right)^{-3} > 1\ , \tag{5.22}$$

and for a dense stellar wind ($s=2$) :

$$\begin{aligned} Q &\simeq 0.19\ f^{-2}\ \left(\frac{E}{10^{53}\ \rm erg}\right)\left(\frac{A}{7.6\ 10^{11}\ \rm g.cm^{-1}}\right)^{-1} \\ &\quad \times \left(\frac{\bar{\Gamma}}{100}\right)^{-4}\left(\frac{t_{\rm w}}{10\ \rm s}\right)^{-1} > 1\ . \end{aligned} \tag{5.23}$$

It is clear that for a uniform medium ($s=0$), except for low external densities, or for low injected total energy E, the deceleration starts at large radii and the reverse shock propagates within a ordered relativistic ejecta where the internal shocks have already disappeared. On the other hand, in the dense stellar wind case ($s=2$), the estimate of Q seems to indicate that in most cases the reverse shock will interact with the internal shocks.

Radiative processes. The same kind of parametrization with $\alpha_{\rm B}$, $\alpha_{\rm e}$ and ζ already made for the external and the internal shocks can be used for the reverse shock. Then it is possible to estimate in the same way the magnetic field, the typical electron Lorentz factor and the synchrotron and/or inverse Compton radiation to compute the contribution of the reverse shock to the observed emission. The main differences between different models are in the assumptions concerning the $\alpha_{\rm B}$ and $\alpha_{\rm e}$ parameters : (i) Sari and Piran [31] adopt the same values than for the external shock. Therefore, as the reverse shock is just midly relativistic, so that the internal energy created in the shocked medium is not so high as in the case of the external shock, the reverse shock radiates at low energy and is observed as an "optical flash", that could explain the ROTSE observations of GRB 990123. (ii) Daigne and

Mochkovitch [56] argue that because of the midly relativistic nature of the reverse shock, this shock is much closer to the internal shocks and they adopt the same parameters than in the internal shock phase. Therefore, when the reverse shock is present in the relativistic ejecta at the same moment than the internal shocks ($Q < 1$), its contribution to the emission is also in the gamma-ray range. When the reverse shock appears later ($Q > 1$), as the density and the magnetic field decrease with the radius, the spectral range goes towards the low energy bands (typically soft X-rays for $Q \gtrsim 1$).

5.3 Results

Uniform external medium : We illustrate the effect of the reverse shock for GRB 960720 in the case of a small density uniform external medium. This single pulse burst has been observed both in X-rays and gamma-rays by Beppo-SAX (see figure 32). It follows the power-law dependence of the pulse width with the energy band [6] not only in the gamma-ray range but also with the same slope down to the soft X-ray bands. The gamma-ray properties of this burst can be easily reproduced by the internal shock model. Figure 33 show the result obtained for $\bar{\Gamma} = 290$, $t_{\mathrm{w}} = 4$ s and $E = 5\ 10^{52}$ erg. It is clear that the pulse width-energy relation is reproduced only in the gamma-ray band, as the X-ray emission stops too early whereas the observations show an X-ray emission perduring after the end of the gamma-ray emission. We then include the contribution of the reverse shock due to an external medium with a uniform density $n = 10\ \mathrm{cm}^{-3}$. This contribution is only detected in X-rays and increase the pulse width in this energy band so that the observed relation is now reproduced (with the correct slope) over the whole spectral range [56].

Dense stellar wind : The case of a dense external medium, for instance due to the presence of a stellar wind, is much more problematic. As Q is now very low, the reverse shock appears very early (possibly even before the internal shocks) and dramatically affect the internal shock phase so that the prompt gamma-ray profile is strongly affected. The temporal and spectral properties of GRBs are therefore no longer reproduced [57]. To avoid this major problem, it is necessary to recover large values of Q. From equation 5.23, this leads to new constraints on the model, (i) either on the environment density profile : if the stellar wind is not so dense, or even better, if it disappears (because of a low metallicity of the progenitor for instance), the deceleration starts later and we come back to the previous case ; (ii) or on the relativistic ejecta : if for instance the energy E increases, the ejecta can more easily penetrate within the external medium and the deceleration starts later [57]. Another possibility would be to decrease $\bar{\Gamma}$ but this is limited by the constraint $\bar{\Gamma} \gtrsim 100$.

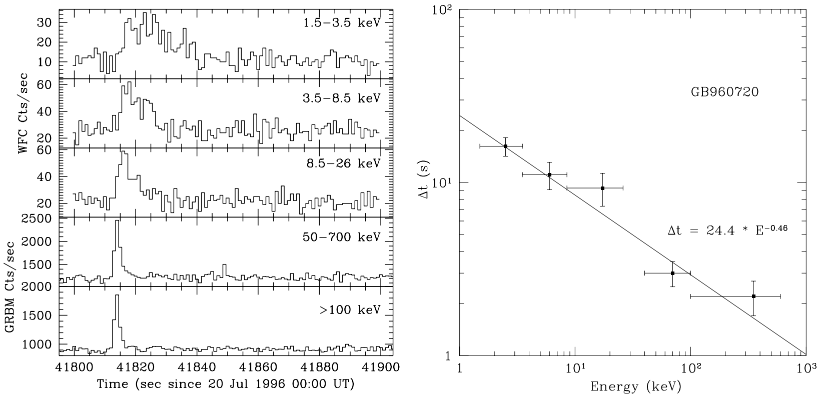

Fig. 32. Beppo-SAX observation of GRB 960720. *Left :* time profile (X- and γ-rays). *Right :* evolution of the pulse width with the energy band. (From [7])

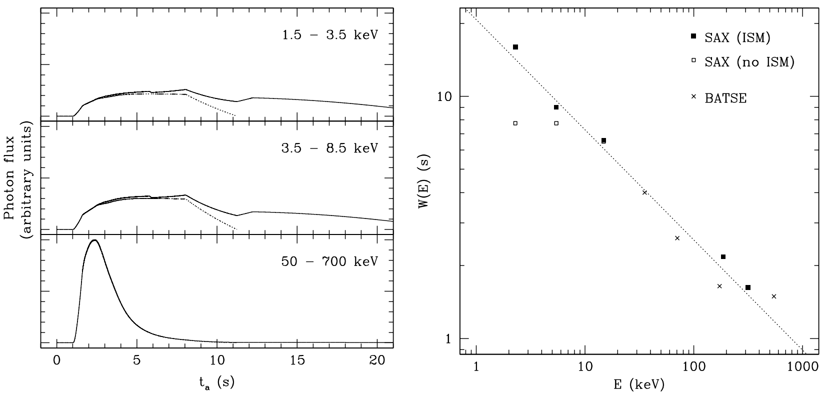

Fig. 33. Simulation of GRB 960720. Both the internal shocks and the reverse shock have been included (solid line). For comparison, the dotted line corresponds to a calculation including the internal shocks only. The effect of the reverse shock is only detected in X-rays and leads to an X-ray emission perduring after the end of the pulse observed in gamma-rays. The correct pulse width–energy relation is then reproduced from the gamma- down to the X-rays. (from [56])

5.4 Photosphere

We close this section on the prompt emission by a brief discussion about the emission produced when the relativistic ejecta becomes transparent at the end of the acceleration phase. According to the estimate of the photospheric radius obtained in section 3, this emission is produced well before the internal shock phase and the deceleration phase (reverse and external shocks). At this radius, the internal energy which is still present can be radiated. The resulting spectrum is close to a blackbody with a temperature that can be derived from the "matter-dominated" regime equations obtained in section 3 :

$$kT_{\mathrm{ph}} \simeq kT_0 \left(\frac{R_{\mathrm{ph}}}{R_{\mathrm{sat}}}\right)^{-2/3} , \tag{5.24}$$

and a luminosity

$$L_{\mathrm{ph}} \simeq \dot{E} \left(\frac{R_{\mathrm{ph}}}{R_{\mathrm{sat}}}\right)^{-2/3} . \tag{5.25}$$

The initial temperature T_0 has been computed in section 3 for an initial radius R_0 assumed to be $6GM_{\mathrm{BH}}/c^2$. It is then possible to estimate the corresponding observed count rate in a given energy band $[E_1, E_2]$:

$$C_{12}^{\mathrm{ph}} = \frac{L_{\mathrm{ph}}}{4\pi D_{\mathrm{L}}^2} \frac{1+z}{kT_{\mathrm{ph}}} \frac{1}{\mathcal{I}_{\mathrm{Planck}}} \int_{(1+z)E_1/kT_{\mathrm{ph}}}^{(1+z)E_2/kT_{\mathrm{ph}}} \frac{x^2}{\exp x - 1} dx , \tag{5.26}$$

where D_{L} is the luminosity distance of the source and $\mathcal{I}_{\mathrm{Planck}} = \pi^4/15$. This has to be compared to the count rate in the same energy band due to the non-thermal emission by internal shocks :

$$C_{12}^{\mathrm{IS}} = \frac{L_{\mathrm{IS}}}{4\pi D_{\mathrm{L}}^2} \frac{1+z}{E_{\mathrm{p}}} \frac{1}{\mathcal{I}_{\mathrm{Band}}} \int_{(1+z)E_1/E_{\mathrm{p}}}^{(1+z)E_2/E_{\mathrm{p}}} \mathcal{B}(x) dx , \tag{5.27}$$

where L_{IS} is the luminosity of the internal shocks, $\mathcal{B}(x)$ is the Band function defined in section 2 and $\mathcal{I}_{\mathrm{Band}}$ the constant $\mathcal{I}_{\mathrm{Band}} = \int_0^{+\infty} x\mathcal{B}(x)dx$. Assuming that $L_{\mathrm{IS}} = f_\gamma \dot{E}$ (f_γ is the efficiency of the internal shocks), we can compute the ratio $R_{12} = C_{12}^{\mathrm{ph}}/C_{12}^{\mathrm{IS}}$ of the two count rates :

$$\begin{aligned} R_{12} \quad \simeq \quad & 1.6 \left(\frac{f_\gamma}{0.1}\right)^{-1} \left(\frac{\dot{E}}{10^{52}\ \mathrm{erg.s^{-1}}}\right)^{-1/4} \left(\frac{M_{\mathrm{BH}}}{10\ \mathrm{M}_\odot}\right)^{1/2} \left(\frac{E_{\mathrm{p}}}{200\ \mathrm{keV}}\right) \\ & \times \frac{\mathcal{I}_{\mathrm{Band}}}{\mathcal{I}_{\mathrm{Planck}}} \frac{\int_{(1+z)E_1/kT_{\mathrm{ph}}}^{(1+z)E_2/kT_{\mathrm{ph}}} \frac{x^2}{\exp x - 1} dx}{\int_{(1+z)E_1/E_{\mathrm{p}}}^{(1+z)E_2/E_{\mathrm{p}}} \mathcal{B}(x) dx} . \end{aligned} \tag{5.28}$$

This ratio is plotted for two energy bands (X- and gamma-rays) and different parameters in figure 34. It is clear that for reasonnable parameters, the thermal photospheric emission dominates or is at least very easily detectable both in X- and gamma-rays. This is of course in contradiction with the observed spectrum of GRBs. The conclusion of this study is that

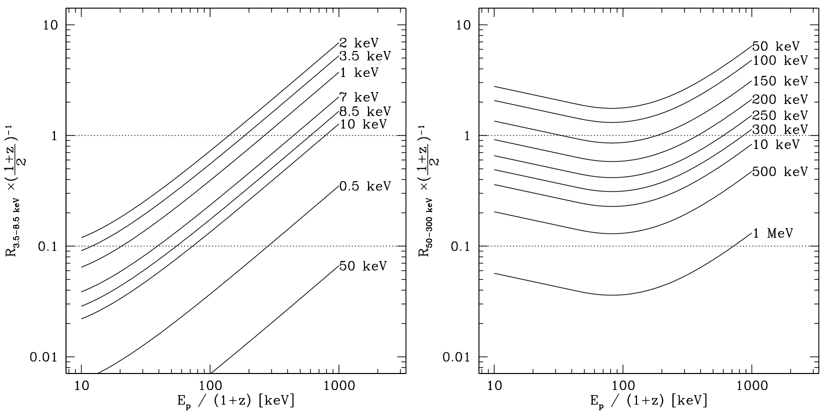

Fig. 34. The ratio of the count rate due to the photospheric emission over the count rate due to the internal shocks as a function of the peak energy of the non-thermal (internal shocks) emission for different values of the temperature (labeled after each curve). *Left :* X-ray band 3.5-8.5 keV ; *Right :* gamma-ray band 50-300 keV. The following parameters have been used : $\dot{E} = 10^{52}$ erg.s^{-1}, $f_\gamma = 0.1$, $M_{\rm BH} = 10$ M$_\odot$. (From [58])

the "standard" fireballs are too hot and luminous. One elegant way that can be proposed to solve the problem is to assume that most of the energy is initially released under magnetic rather than thermal form. In a cold MHD outflow, the reservoir of internal energy when the matter becomes transparent can be much lower than in the previous calculation. Simple estimates show that if only a few percents of the initial energy released is in thermal energy form, the thermal-over-non-thermal radiation ratio R_{12} becomes small enough to be in agreement with the observations [58].

6 Central engine

The physics of the central engine in GRBs is probably the less understood among the three steps of the scenario described in section 3. We recall here the main requirements for the sources : (i) they must be located at cosmological distance with $\langle z\rangle \gtrsim 1$; (ii) they must be compatible with a GRB rate $\mathcal{R}_{\rm GRB}$ of about (see section 3)

$$\mathcal{R}_{\rm GRB} \simeq 5\ 10^{-4} \left(\frac{\left\langle\left(\frac{\Omega}{4\pi}\right)^{-1}\right\rangle}{500}\right)\ \mathcal{R}_{\rm SN}\ , \qquad (6.1)$$

where current estimates of the beaming factor $\left\langle \left(\frac{\Omega}{4\pi}\right)^{-1} \right\rangle$ are about 500 with a large uncertainty [33] ; (iii) they must be able to release a huge energy of about

$$E \simeq 10^{52} \left(\frac{f_\gamma}{0.1}\right) \left(\frac{\langle \Omega/4\pi E_{\gamma,4\pi} \rangle}{10^{51}\ \mathrm{erg}}\right)\ \mathrm{erg}\ , \tag{6.2}$$

where estimates of the efficiency for the conversion to gamma-rays differ among the models but is probably less than 10 % for internal shocks. The estimate of the true energy released in gamma-rays, $\Omega/4\pi E_{\gamma,4\pi}$, also suffers large uncertainties associated to the measure of the beaming factor ; (iv) this energy must be injected in an almost baryon-free flow so that it can accelerate up to high Lorentz factors with $\bar{\Gamma} \gtrsim 100$. An additionnal requirement in the context of the internal shock model is that the source must vary on short timescales (1 ms) and the process of relativistic ejection must last for at least the typical observed duration of GRBs.

It is clear that such requirements make the question extremely complex. Only a few answers have been proposed and most of them have not yet been studied in detailed simulations. We summarize below the two main proposals : (i) merger of two compact objects ; (iii) gravitational collapse of very massive stars into black holes.

6.1 Mergers

The coalescence of a binary system of two neutron stars [59, 60] and the merger of a neutron star – black hole system [61, 62] have been proposed as a possible source for GRBs. The product of the merger is a black hole ($M_{\mathrm{BH}} \sim 2.5\ \mathrm{M}_\odot$) surrounded by a debris torus ($m \lesssim 0.1\ \mathrm{M}_\odot$) which appears to satisfy some of the requirements : (i) the variability time scale is correct, as the dynamical timescale at the inner edge of the torus is $\lesssim 1$ ms ; (ii) the region along the rotation axis is almost baryon-free which offers a nice possibility to have ejections with small baryonic load ; (iii) the environment is very clean with a probably low density which favors the acceleration up to high Lorentz factors and corresponds to a late deceleration so that the reverse shock does not suppress the internal shock phase. However this proposal also suffers from severe problems : (i) the known rate of mergers is probably too low, except if $\left\langle (\Omega/4\pi)^{-1} \right\rangle$ has been overestimated ; (ii) the energy reservoir (rotation of the black hole + accretion from the torus to the hole) is probably too low for the most luminous GRBs ; (iii) mergers are supposed to occur at large distance from the central regions of the host galaxy as there is a long delay between the binary system formation and the coalescence, whereas observations of afterglows show evidences in favor of an association with the star-forming central regions. However all these elements prove that mergers still remain possible model for short duration

GRBs, for which no optical afterglow has never be found.

6.2 Collapsars

The collapse of a very massive star into a black hole, sometimes called a "failed supernova" [63] or an "hypernova" [64], is another possibility which solves some of the problems of the previous model and is obviously favored for the long-duration GRBs from the observational evidences of an association with star-forming regions. In the center of the collapsing object, a black hole + thick disk system is also formed, with the difference that the black hole can be more massive (10 $M_{\odot}$ or even more) and the torus is feeded with the still falling material coming from the external layers of the progenitor. The main advantages are that the rate of massive star collapses, for reasonable estimates of the critical mass above which a black hole is formed, is much higher than the GRB rate, even for large $\left\langle(\Omega/4\pi)^{-1}\right\rangle$ factors and that the energy reservoir is much larger than in mergers. Two problems are that it is certainly more difficult to accelerate matter inside an infalling star than in empty space and that the environment, except for low metallicity progenitors, should be dominated by the dense wind of the massive star, which is not supported by the observations as explained in sections 4 and 5.

6.3 MHD winds ?

The neutrino-antineutrino annihilation along the rotation axis of the system, i.e. in a region widely depleted from baryons due to the centrifugal forces, may be the process at the origin of the energy injection in GRBs [62, 65, 66] but this possibility has probably to be considered for short GRBs only ($\lesssim 1$ s) as this process seems to be too unefficient to work for long bursts [67]. It is then often proposed that the solution could be a magnetic outflow [40, 53, 68] where the energy of the disk and/or the black hole (via the Blandford-Znajek effect [69]) is extracted by a strong magnetic field ($B \sim 10^{15}$ G). No numerical simulations of such a mechanism in the GRB context are available. Several important questions are still to be asked : (i) how can the magnetic energy be converted into kinetic energy (reconnection at large distance ?) and is the process efficient enough ? [70] ; (ii) is it possible with such a mechanism to have a low baryonic pollution ? Some recent estimates show that it is probably very difficult in the case of an outflow coming from the disk [39]. It is probably much easier with the Blandford-Znajek effect, as long as the flow is not polluted by material coming from the disk ; (iii) is the propagation of the outflow in the collapsing star possible so that it reaches terminal Lorentz factors larger than 100 : recent simulations indicate that it is difficult but probably possible [71, 72].

7 More than photons ?

The non-photonic emission of GRBs is very briefly discussed in this section.

7.1 Ultra-high energy cosmic rays

During the internal shock phase, the presence of several shocks propagating within the relativistic ejecta favors the acceleration of particles. It is possible to make basic estimates of the maximum energy $E_{\rm max}$ that one given type of particle can get (this maximum energy is reached when the acceleration time becomes longer than the radiative time and/or the escape time). For protons, with reasonable parameters regarding the size of the shells and the magnetic field, $E_{\rm max}$ can be as high as 10^{19}–10^{20} eV (see e.g. [73]). Therefore GRBs appear as possible candidates for the origin of UHECRs (ultra-high energy cosmic rays). However, even if GRBs have the ability to accelerate protons up to very high energies (which has still to be investigated in details), another difficulty is that the origin of UHECRs above the GZK cutoff is necessarily local, within a distance of about 100 Mpc. The local rate of GRBs is very poorly known but certainly low. Then it has to be tested that the observations, especially the coming detections by the AUGER observatory, will be compatible with only one or two local sources.

7.2 High energy neutrinos

During the internal shock phase, if protons are accelerated, they can interact with gamma-ray photons to produce pions, decaying in muons and neutrinos (see e.g. [73]). This is independent from the production of UHECRs as protons of only $\sim 10^{16}$ eV (!) are required to produce $\sim 10^{14}$ eV neutrinos by photo-meson interaction with MeV photons. Such neutrinos can be detected by experiments like ANTARES, IceCube, AMANDA, etc. However, current estimates of the expected number of neutrinos from GRBs are not very optimistic, typically a few per year...

7.3 Gravitational waves

The main hope for the detection of gravitational waves in association with GRBs is the possibility that short GRBs ($\lesssim 1$ s) are related to compact object mergers. This justifies an important effort in the coming years to better study this subclass of bursts and identify their progenitors. Concerning the long bursts, it is very unlikely that a signal of gravitational waves can be detected with the current experiments, as the expected gravitational wave production during an (even very) asymmetric collapse of a massive star is much weaker than for a coalescence.

8 Conclusions

To conclude this lecture which is a short introduction to GRBs, I briefly list a few questions that will have to be investigated in the coming years. A first series of questions are related to the prompt emission, and especially to the spectral properties :

• What is the high-energy emission ? This will be studied with several instruments (AGILE, GLAST, HESS, ...). If a cutoff in the high-energy power-law can be identified, it will provide a direct measure of the Lorentz factor of the emitting material (see section 3). If the main peak observed in the gamma-ray range is due to synchrotron radiation, the identification of a second peak at high energy, due to inverse Compton scattering, would lead to the measure of important parameters such as the magnetic field and the Lorentz factor of the electrons. If the radiative process at work in GRBs is not the SSC process, the extension of the spectrum possibly up to 300 GeV would greatly help in its indentification.
• The detection of high-energy neutrinos from a (probably bright and close) GRB would be of great interest. This would provide completely new information on the processes operating in GRBs, especially on the acceleration of particles by relativistic shock waves.
• What is the optical spectrum ? Only one detection of the optical prompt emission has ever been made, in GRB 990123 by ROTSE. It is a great challenge for the next generation of robotic telescopes as ARAGO [74] or for future satellites as ECLAIRs [75] to increase this number to better constraint the theoretical interpretation of the GRB optical flashes.
• Will the narrow distribution of the peak energy E_{p} observed by BATSE be confirmed by the current and future missions (HETE-2, INTEGRAL, SWIFT). Are the X-ray flashes observed by Beppo-SAX [76] and HETE-2 [77] a peculiar class of intrinsically softer GRBs ?
• Do GRBs have precursors in the X-ray or optical energy ranges ? Such precursors will be searched by the future satellite ECLAIRs [75].

A second series of questions are related to the afterglow :

• Is it possible to use the almost real-time GRB alerts that are now available to perform a rapid multi-wavelength follow-up of the early afterglow. During this phase, the afterglow is probably very bright even at large redshift, which makes GRBs promising tools to explore the very distant Universe. A related question is the capability to do rapid infrared observations to detect GRB afterglows at very high redshift ($z \gtrsim 6$).
• When does the afterglow start and in which energy band does it initially peak ? Early afterglow observations would give very strong constraints on

the energetics of the burst and on the density profile of the environment. It is also important to understand the transition between the burst and the afterglow.
• What is the distribution of the long GRB redshifts ? This is of course the main result expected from SWIFT. This observation in association with a better identification of the GRB progenitors would allow to trace the star-formation rate with GRBs.
• Is it possible to better constrain the beaming factor in GRBs ? This is a fundamental parameter to know the true energy budget of the GRB phenomenon and the true rate of events. A very promising possibility is the search for orphan afterglows in large surveys. If one is able to detect afterglows off-axis, when the initial GRB was not observed, a comparison of the event rates would give a completely independant determination of the beaming factor.
• Can the GRB-supernova association be confirmed by new observations ? This would have a strong impact on the models of GRB progenitors.
• Do short GRBs ($\lesssim 1$ s) have afterglows and what are their progenitors? The answer could come from the location of the afterglow, either in star-forming regions or at the periphery of their host galaxies ?

All these questions show that the GRB field has a very promising future, especially if it is confirmed that GRBs can occur at very high redshift. They would allow to search for the reionization epoch, and for population III stars, to trace the star-formation rate up to high redshifts, to study the intergalactic medium, etc... GRBs may then become a unique tool to probe the very distant Universe.

It is a pleasure to thank Robert Mochkovitch for his careful reading of this manuscript.

References

[1] R. W. Klebesadel, I. B. Strong, and R. A. Olson. Observations of Gamma-Ray Bursts of Cosmic Origin. *ApJ*, 182:L85–L88, 1973.

[2] W. S. Paciesas, C. A. Meegan, G. N. Pendleton, M. S. Briggs, C. Kouveliotou, T. M. Koshut, J. P. Lestrade, M. L. McCollough, J. J. Brainerd, J. Hakkila, W. Henze, R. D. Preece, V. Connaughton, R. M. Kippen, R. S. Mallozzi, G. J. Fishman, G. A. Richardson, and M. Sahi. The Fourth BATSE Gamma-Ray Burst Catalog (Revised). *ApJS*, 122:465–495, 1999.

[3] R. J. Nemiroff. A Century of Gamma-Ray Burst Models. In *AIP Conf. Proc. 307: Gamma-Ray Bursts*, pages 730–734, 1994.

[4] J.-P. Dezalay, J. P. Lestrade, C. Barat, R. Talon, O. Terekhov, R. Synaev, and A. Kuznetsov. Comparison of the Properties of Short and Long Gamma-Ray Bursts Observed with PHEBUS. In *Gamma-ray bursts, Proceedings of the 3rd Huntsville Symposium, AIP Conference Proceedings Series vol. 384, edited by C. Kouveliotou, M.F. Briggs, and G.J. Fishman*, pages 37–41, 1996.

[5] C. Kouveliotou, C. A. Meegan, G. J. Fishman, N. P. Bhat, M. S. Briggs, T. M. Koshut, W. S. Paciesas, and G. N. Pendleton. Identification of two classes of gamma-ray bursts. *ApJ*, 413:L101–L104, 1993.

[6] J. P. Norris, R. J. Nemiroff, J. T. Bonnell, J. D. Scargle, C. Kouveliotou, W. S. Paciesas, C. A. Meegan, and G. J. Fishman. Attributes of Pulses in Long Bright Gamma-Ray Bursts. *ApJ*, 459:393–412, 1996.

[7] L. Piro, J. Heise, R. Jager, E. Costa, F. Frontera, M. Feroci, J. M. Muller, L. Amati, M. N. Cinti, D. dal Fiume, L. Nicastro, M. Orlandini, and G. Pizzichini. The first X-ray localization of a gamma -ray burst by BeppoSAX and its fast spectral evolution. *A&A*, 329:906–910, 1998.

[8] R. D. Preece, M. S. Briggs, R. S. Mallozzi, G. N. Pendleton, W. S. Paciesas, and D. L. Band. The BATSE Gamma-Ray Burst Spectral Catalog. I. High Time Resolution Spectroscopy of Bright Bursts Using High Energy Resolution Data. *ApJS*, 126:19–36, 2000.

[9] M. S. Briggs, D. L. Band, R. M. Kippen, R. D. Preece, C. Kouveliotou, J. van Paradijs, G. H. Share, R. J. Murphy, S. M. Matz, A. Connors, C. Winkler, M. L. McConnell, J. M. Ryan, O. R. Williams, C. A. Young, B. Dingus, J. R. Catelli, and R. A. M. J. Wijers. Observations of GRB 990123 by the Compton Gamma Ray Observatory. *ApJ*, 524:82–91, 1999.

[10] D. Band, J. Matteson, L. Ford, B. Schaefer, D. Palmer, B. Teegarden, T. Cline, M. Briggs, W. Paciesas, G. Pendleton, G. Fishman, C. Kouveliotou, C. Meegan, R. Wilson, and P. Lestrade. BATSE observations of gamma-ray burst spectra. I - Spectral diversity. *ApJ*, 413:281–292, 1993.

[11] A. Crider, E. P. Liang, R. D. Preece, M. S. Briggs, G. N. Pendleton, W. S. Paciesas, D. L. Band, and J. L. Matteson. The hardness evolution of gamma-ray burst pulses. *A&AS*, 138:401–402, 1999.

[12] V. E. Kargatis, E. P. Liang, and BATSE Team. Spectral Evolution of GRB Pulses. *Ap&SS*, 231:177–180, 1995.

[13] E. Liang and V. Kargatis. Dependence of the spectral evolution of gamma-ray bursts on their photon fluence. *Nature*, 381:49–51, 1996.

[14] F. Ryde and R. Svensson. On the Time Evolution of Gamma-Ray Burst Pulses: A Self-Consistent Description. *ApJ*, 529:L13–L16, 2000.

[15] F. Ryde and R. Svensson. On the Variety of the Spectral and Temporal Behavior of Long Gamma-Ray Burst Pulses. *ApJ*, 566:210–228, 2002.

[16] C. Akerlof, R. Balsano, S. Barthelemy, J. Bloch, P. Butterworth, D. Casperson, T. Cline, S. Fletcher, F. Frontera, G. Gisler, J. Heise, J. Hills, R. Kehoe, B. Lee, S. Marshall, T. McKay, R. Miller, L. Piro, W. Priedhorsky, J. Szymanski, and J. Wren. Observation of contemporaneous optical radiation from a gamma-ray burst. *Nature*, 398:400–402, 1999.

[17] P. J. Groot, T. J. Galama, J. van Paradijs, R. Strom, J. Telting, R. G. M. Rutten, M. Pettini, N. Tanvir, R. Naber, C. Kouveliotou, J. in 't Zand, J. Heise, E. Costa, M. Feroci, L. Piro, F. Frontera, G. Zavattini, L. Nicastro, and E. Palazzi. GRB 970228. *IAU Circ.*, 6584, 1997.

[18] A. S. Fruchter, E. Pian, S. E. Thorsett, L. E. Bergeron, R. A. González, M. Metzger, P. Goudfrooij, K. C. Sahu, H. Ferguson, M. Livio, M. Mutchler, L. Petro, F. Frontera, T. Galama, P. Groot, R. Hook, C. Kouveliotou, D. Macchetto, J. van Paradijs, E. Palazzi, H. Pedersen, W. Sparks, and M. Tavani. The Fading Optical Counterpart of GRB 970228, 6 Months and 1 Year Later. *ApJ*, 516:683–692, 1999.

[19] A. Panaitescu and P. Kumar. Fundamental Physical Parameters of Collimated Gamma-Ray Burst Afterglows. *ApJ*, 560:L49–L53, 2001.

[20] T. J. Galama, P. M. Vreeswijk, J. van Paradijs, C. Kouveliotou, T. Augusteijn, H. Bohnhardt, J. P. Brewer, V. Doublier, J.-F. Gonzalez, B. Leibundgut, C. Lidman, O. R. Hainaut, F. Patat, J. Heise, J. in 't Zand, K. Hurley, P. J. Groot,

R. G. Strom, P. A. Mazzali, K. Iwamoto, K. Nomoto, H. Umeda, T. Nakamura, T. R. Young, T. Suzuki, T. Shigeyama, T. Koshut, M. Kippen, C. Robinson, P. de Wildt, R. A. M. J. Wijers, N. Tanvir, J. Greiner, E. Pian, E. Palazzi, F. Frontera, N. Masetti, L. Nicastro, M. Feroci, E. Costa, L. Piro, B. A. Peterson, C. Tinney, B. Boyle, R. Cannon, R. Stathakis, E. Sadler, M. C. Begam, and P. Ianna. An unusual supernova in the error box of the gamma-ray burst of 25 April 1998. *Nature*, 395:670–672, 1998.

[21] M. R. Metzger, S. G. Djorgovski, S. R. Kulkarni, C. C. Steidel, K. L. Adelberger, D. A. Frail, E. Costa, and F. Frontera. Spectral constraints on the redshift of the optical counterpart to the gamma-ray burst of 8 May 1997. *Nature*, 387:878–880, 1997.

[22] J. S. Bloom, S. G. Djorgovski, S. R. Kulkarni, and D. A. Frail. The Host Galaxy of GRB 970508. *ApJ*, 507:L25–L28, 1998.

[23] S. G. Djorgovski, S. R. Kulkarni, J. S. Bloom, D. A. Frail, F. A. Harrison, T. J. Galama, D. Reichart, S. M. Castro, D. Fox, R. Sari, E. Berger, P. Price, S. Yost, R. Goodrich, and F. Chaffee. The GRB Host Galaxies and Redshifts. In *Gamma-ray Bursts in the Afterglow Era, Proceedins of the 2nd Workshop held in Rome, October 2000, edited by E. Costa, F. Frontera and J. Hjorth*, pages 218–225, 2001.

[24] J. S. Bloom, S. R. Kulkarni, and S. G. Djorgovski. The Observed Offset Distribution of Gamma-Ray Bursts from Their Host Galaxies: A Robust Clue to the Nature of the Progenitors. *AJ*, 123:1111–1148, 2002.

[25] A. M. Beloborodov. Neutron-Fed Afterglows of Gamma-Ray Bursts. *to be published in ApJ Letters*, astro-ph/0209228, 2002.

[26] T. J. Galama, N. Tanvir, P. M. Vreeswijk, R. A. M. J. Wijers, P. J. Groot, E. Rol, J. van Paradijs, C. Kouveliotou, A. S. Fruchter, N. Masetti, H. Pedersen, B. Margon, E. W. Deutsch, M. Metzger, L. Armus, S. Klose, and B. Stecklum. Evidence for a Supernova in Reanalyzed Optical and Near-Infrared Images of GRB 970228. *ApJ*, 536:185–194, 2000.

[27] L. Piro, G. Garmire, M. Garcia, G. Stratta, E. Costa, M. Feroci, P. Mészáros, M. Vietri, H. Bradt, D. Frail, F. Frontera, J. Halpern, J. Heise, K. Hurley, N. Kawai, R. M. Kippen, F. Marshall, T. Murakami, V. V. Sokolov, T. Takeshima, and A. Yoshida. Observation of X-ray Lines from a Gamma-Ray Burst (GRB991216): Evidence of Moving Ejecta from the Progenitor. *Science*, 290:955–958, 2000.

[28] J. N. Reeves, D. Watson, J. P. Osborne, K. A. Pounds, P. T. O'Brien, A. D. T. Short, M. J. L. Turner, M. G. Watson, K. O. Mason, M. Ehle, and N. Schartel. The signature of supernova ejecta in the X-ray afterglow of the γ-ray burst 011211. *Nature*, 416:512–515, 2002.

[29] S. Covino, D. Lazzati, G. Ghisellini, P. Saracco, S. Campana, G. Chincarini, S. di Serego, A. Cimatti, L. Vanzi, L. Pasquini, F. Haardt, G. L. Israel, L. Stella, and M. Vietri. GRB 990510: linearly polarized radiation from a fireball. *A&A*, 348:L1–L4, 1999.

[30] R. A. M. J. Wijers, P. M. Vreeswijk, T. J. Galama, E. Rol, J. van Paradijs, C. Kouveliotou, T. Giblin, N. Masetti, E. Palazzi, E. Pian, F. Frontera, L. Nicastro, R. Falomo, P. Soffitta, and L. Piro. Detection of Polarization in the Afterglow of GRB 990510 with the ESO Very Large Telescope. *ApJ*, 523:L33–L36, 1999.

[31] R. Sari and T. Piran. GRB 990123: The Optical Flash and the Fireball Model. *ApJ*, 517:L109–L112, 1999.

[32] C. Porciani and P. Madau. On the Association of Gamma-Ray Bursts with Massive Stars: Implications for Number Counts and Lensing Statistics. *ApJ*, 548:522–531, 2001.

[33] D. A. Frail, S. R. Kulkarni, R. Sari, S. G. Djorgovski, J. S. Bloom, T. J. Galama, D. E. Reichart, E. Berger, F. A. Harrison, P. A. Price, S. A. Yost, A. Diercks, R. W.

Goodrich, and F. Chaffee. Beaming in Gamma-Ray Bursts: Evidence for a Standard Energy Reservoir. *ApJ*, 562:L55–L58, 2001.

[34] J. M. Kommers, W. H. G. Lewin, C. Kouveliotou, J. van Paradijs, G. N. Pendleton, C. A. Meegan, and G. J. Fishman. The Intensity Distribution of Faint Gamma-Ray Bursts Detected with BATSE. *ApJ*, 533:696–709, 2000.

[35] T. Piran. Gamma-ray bursts and the fireball model. *Physics Reports*, 314:575–667, 1999.

[36] Y. Lithwick and R. Sari. Lower Limits on Lorentz Factors in Gamma-Ray Bursts. *ApJ*, 555:540–545, 2001.

[37] B. Paczynski. Gamma-ray bursters at cosmological distances. *ApJ*, 308:L43–L46, 1986.

[38] J. Goodman. Are gamma-ray bursts optically thick? *ApJ*, 308:L47–L50, 1986.

[39] F. Daigne and R. Mochkovitch. Baryonic pollution in gamma-ray bursts: The case of a magnetically driven wind emitted from a disk orbiting a stellar mass black hole. *A&A*, 388:189–201, 2002.

[40] P. Meszaros and M. J. Rees. Poynting Jets from Black Holes and Cosmological Gamma-Ray Bursts. *ApJ*, 482:L29–L32, 1997.

[41] R. D. Blandford and C. F. McKee. Fluid dynamics of relativistic blast waves. *Physics of Fluids*, 19:1130–1138, 1976.

[42] A. Panaitescu and P. Kumar. Analytic Light Curves of Gamma-Ray Burst Afterglows: Homogeneous versus Wind External Media. *ApJ*, 543:66–76, 2000.

[43] G. B. Rybicki and A. P. Lightman. *Radiative processes in astrophysics.* New York, Wiley-Interscience, 393 pages, 1979.

[44] R. Sari, T. Piran, and R. Narayan. Spectra and Light Curves of Gamma-Ray Burst Afterglows. *ApJ*, 497:L17–20, 1998.

[45] J. E. Rhoads. How to Tell a Jet from a Balloon: A Proposed Test for Beaming in Gamma-Ray Bursts. *ApJ*, 487:L1–L4, 1997.

[46] A. Panaitescu and P. Kumar. Jet Energy and Other Parameters for the Afterglows of GRB 980703, GRB 990123, GRB 990510, and GRB 991216 Determined from Modeling of Multifrequency Data. *ApJ*, 554:667–677, 2001.

[47] S. Ayal and T. Piran. Remnants from Gamma-Ray Bursts. *ApJ*, 555:23–30, 2001.

[48] M. J. Rees and P. Meszaros. Unsteady outflow models for cosmological gamma-ray bursts. *ApJ*, 430:L93–L96, 1994.

[49] F. Daigne and R. Mochkovitch. Gamma-ray bursts from internal shocks in a relativistic wind: temporal and spectral properties. *MNRAS*, 296:275–286, 1998.

[50] F. Daigne and R. Mochkovitch. Gamma-ray bursts from internal shocks in a relativistic wind: a hydrodynamical study. *A&A*, 358:1157–1166, 2000.

[51] S. Kobayashi, T. Piran, and R. Sari. Can Internal Shocks Produce the Variability in Gamma-Ray Bursts? *ApJ*, 490:92–98, 1997.

[52] A. M. Bykov and P. Meszaros. Electron Acceleration and Efficiency in Nonthermal Gamma-Ray Sources. *ApJ*, 461:L37–L40, 1996.

[53] H. C. Spruit, F. Daigne, and G. Drenkhahn. Large scale magnetic fields and their dissipation in GRB fireballs. *A&A*, 369:694–705, 2001.

[54] F. Daigne and R. Mochkovitch. The physics of pulses in gamma-ray bursts: temporal profiles, time lags and emission processes. *submitted to MNRAS*, 2002.

[55] R. Sari and T. Piran. Hydrodynamic Timescales and Temporal Structure of Gamma-Ray Bursts. *ApJ*, 455:L143–L146, 1995.

[56] F. Daigne and R. Mochkovitch. Theoretical interpretation of the X-ray properties of GRB 960720. *A&AS*, 138:523–524, 1999.

[57] F. Daigne and R. Mochkovitch. Interaction between Internal Shocks and the Reverse Shock for a GRB in a Dense Stellar Wind. In *Gamma-ray Bursts in the Afterglow Era, Proceedins of the 2nd Workshop held in Rome, October 2000, edited by E. Costa, F. Frontera and J. Hjorth*, pages 324–327, 2001.

[58] F. Daigne and R. Mochkovitch. The expected thermal precursors of gamma-ray bursts in the internal shock model. *MNRAS*, 336:1271–1280, 2002.

[59] D. Eichler, M. Livio, T. Piran, and D. N. Schramm. Nucleosynthesis, neutrino bursts and gamma-rays from coalescing neutron stars. *Nature*, 340:126–128, 1989.

[60] B. Paczynski. Cosmological gamma-ray bursts. *Acta Astronomica*, 41:257–267, 1991.

[61] R. Narayan, B. Paczynski, and T. Piran. Gamma-ray bursts as the death throes of massive binary stars. *ApJ*, 395:L83–L86, 1992.

[62] R. Mochkovitch, M. Hernanz, J. Isern, and X. Martin. Gamma-ray bursts as collimated jets from neutron star/black hole mergers. *Nature*, 361:236–238, 1993.

[63] S. E. Woosley. Gamma-ray bursts from stellar mass accretion disks around black holes. *ApJ*, 405:273–277, 1993.

[64] B. Paczynski. Are Gamma-Ray Bursts in Star-Forming Regions? *ApJ*, 494:L45–L48, 1998.

[65] P. Meszaros and M. J. Rees. High-entropy fireballs and jets in gamma-ray burst sources. *MNRAS*, 257:29P–31P, 1992.

[66] R. Mochkovitch, M. Hernanz, J. Isern, and S. Loiseau. Gamma-ray bursts from relativistic beams in neutron star mergers. *A&A*, 293:803–809, 1995.

[67] M. Ruffert, H.-T. Janka, K. Takahashi, and G. Schaefer. Coalescing neutron stars - a step towards physical models. II. Neutrino emission, neutron tori, and gamma-ray bursts. *A&A*, 319:122–153, 1997.

[68] C. Thompson. A Model of Gamma-Ray Bursts. *MNRAS*, 270:480–498, 1994.

[69] R. D. Blandford and R. L. Znajek. Electromagnetic extraction of energy from Kerr black holes. *MNRAS*, 179:433–456, 1977.

[70] F. Daigne and G. Drenkhahn. Stationary equatorial MHD flows in general relativity. *A&A*, 381:1066–1079, 2002.

[71] M. A. Aloy, E. Müller, J. M. Ibáñez, J. M. Martí, and A. MacFadyen. Relativistic Jets from Collapsars. *ApJ*, 531:L119–L122, 2000.

[72] A. I. MacFadyen, S. E. Woosley, and A. Heger. Supernovae, Jets, and Collapsars. *ApJ*, 550:410–425, 2001.

[73] E. Waxman. High-Energy Particles from γ-Ray Bursts. In *Lecture Notes in Physics, vol. 576: Physics and Astrophysics of UHECRs*, page 122, 2001.

[74] M. Boër. Agile telescopes to monitor optical transients and sky variability: From TAROT to ARAGO. *Astronomische Nachrichten*, 322:343–346, 2001.

[75] J. Paul, D. Barret, and The Eclairs Collaboration. ECLAIRs: A Microsatellite for the Multiwavelength Observation of the Prompt Emission of Gamma-Ray Bursts. In *SF2A-2002: Semaine de l'Astrophysique Francaise*, 2002.

[76] J. Heise, J. in't Zand, R. M. Kippen, and P. M. Woods. X-Ray Flashes and X-Ray Rich Gamma Ray Bursts. In *Gamma-ray Bursts in the Afterglow Era, Proceedins of the 2nd Workshop held in Rome, October 2000, edited by E. Costa, F. Frontera and J. Hjorth*, pages 16–21, 2001.

[77] C. Barraud, J. Olive, J. P. Lestrade, J. Atteia, K. Hurley, G. Ricker, D. Q. Lamb, N. Kawai, M. Boer, J. Dezalay, G. Pizzichini, R. Vanderspek, G. Crew, J. Doty, G. Monelly, J. Villasenor, N. Butler, A. Levine, A. Yoshida, Y. Shirasaki, T. Sakamoto, T. Tamagawa, K. Torii, M. Matsuoka, E. E. Fenimore, M. Galassi, T. Tavenner, T. Q. Donaghy, C. Graziani, and J. G. Jernigan. Spectral analysis of 24 GRBs/XRFs observed with HETE-2/FREGATE. *to be published in A&A*, astro-ph/0206380, 2002.